Research Square

Preprints are preliminary reports that have not undergone peer review.
They should not be considered conclusive, used to inform clinical practice,
or referenced by the media as validated information.

Multidimensional Mechanistic Elucidation of Panax Notoginseng Saponins for Alcohol-Induced Osteonecrosis of the Femoral Head: Integrating Network Pharmacology, Molecular Dynamics Simulation and In Vivo Validation

Ruokun Bai
Guangxi University of Chinese Medicine, Nanning, China
Hua Su
.Guangxi Institute of Chinese Medicine&Pharmaceutical Science, Nanning, China
Jian Mo
mj4587537260126.com

Guangxi University of Chinese Medicine, Nanning, China
Xiaoyun Zhang
Guangxi University of Chinese Medicine, Nanning, China
Zhengpeng Li
Guangxi University of Chinese Medicine, Nanning, China
Xiangshan Chen
Ruikang Affiliated Hospital of Guangxi University of Chinese Medicine, Nanning, China
Sentao Ye
Guilin Hospital of Traditional Chinese Medicine, Nanning, China
Xiayu Nie
Guangxi University of Chinese Medicine, Nanning, China
Shuai Chen
Guangxi University of Chinese Medicine, Nanning, China

Research Article

Keywords: Network Pharmacology, Molecular Dynamics Simulation, Panax Notoginseng Saponins, Alcohol-Induced Osteonecrosis of the Femoral Head, Machine Learning, Osteocyte Apoptosis

Posted Date: July 2nd, 2026

DOI: https://doi.org/10.21203/rs.3.rs-10193250/v1

License: This work is licensed under a Creative Commons Attribution 4.0 International License.
Read Full License

Additional Declarations: The authors declare no competing interests.

Multidimensional Mechanistic Elucidation of Panax Notoginseng Saponins for Alcohol-Induced Osteonecrosis of the Femoral Head: Integrating Network Pharmacology, Molecular Dynamics Simulation and In Vivo Validation

Ruokun Bai[1,2], Hua Su[3,5], Jian Mo[1,2], Xiaoyun Zhang[1,2], Zhengpeng Li[1,2], Xiangshan Chen[2], Sentao Ye[4], Xiayu Nie[1,2], Shuai Chen[1,2], Bing Liang[3]

Corresponding author：
1.Jian Mo,Email Address：mj458753726@126.com
2.Bing Liang,Email Address：462712902@qq.com

Affiliated institutions
1. Guangxi University of Chinese Medicine, Nanning, China
2. Ruikang Affiliated Hospital of Guangxi University of Chinese Medicine, Nanning, China
3.Guangxi Institute of Chinese Medicine&Pharmaceutical Science, Nanning, China
4.Guilin Hospital of Traditional Chinese Medicine, Nanning, China
5.Guangxi Key Laboratory of Traditional Chinese Medicine Quality Standards, nanning, China

Abstract

Background: Alcohol-induced osteonecrosis of the femoral head (AIONFH) is a prevalent orthopedic disease caused by chronic alcohol abuse, characterized by impaired femoral head perfusion, osteocyte necrosis and progressive structural collapse. Existing hip-preserving interventions yield limited efficacy, with most patients ultimately requiring total hip arthroplasty. Panax Notoginseng Saponins (PNS), the principal bioactive constituents of Panax notoginseng, exhibit pro-angiogenic and anti-osteocyte apoptotic activities; however, its precise therapeutic mechanism against AIONFH remains poorly defined.

Objective: This study aimed to identify the active ingredients, core therapeutic targets and critical signaling pathways of PNS against AIONFH via integrating network pharmacology, molecular dynamics simulation and in vivo animal experiments, validate its therapeutic efficacy, and provide a scientific foundation for its clinical translation.

Methods: PNS active components and their corresponding targets, as well as AIONFH-related targets, were screened from authoritative databases. Intersection targets were subjected to protein-protein interaction (PPI) network construction, and core targets were identified via three machine learning algorithms, followed by Gene

Ontology (GO) and Kyoto Encyclopedia of Genes and Genomes (KEGG) enrichment analyses. Molecular docking was conducted between core targets and PNS active ingredients, and 100 ns molecular dynamics simulation was performed using GROMACS 2022 to assess the stability of protein-ligand complexes. AIONFH rat models were established and treated with PNS via intragastric administration for 4 weeks; pathological staining, immunofluorescence and quantitative real-time PCR (qPCR) were utilized for biological detection.
Results and Discussion: Network pharmacology analysis identified 127 potential targets of PNS, and 18 overlapping targets were obtained by intersecting with 672 AIONFH-related targets. Six core targets (e.g., FGF2, HSD11B1) were screened out, and KEGG analysis revealed the vascular endothelial growth factor (VEGF) pathway as the pivotal signaling cascade. Ginsenoside Re exhibited the strongest binding affinity to HSD11B1 with a binding energy of -12.4 kcal/mol, and 100 ns molecular dynamics simulation verified the conformational stability of the Ginsenoside Re-HSD11B1 complex. In vivo experiments demonstrated that PNS ameliorated trabecular bone microstructure and modulated osteocyte function. Collectively, PNS exerts therapeutic effects on AIONFH through a multi-component, multi-target and multi-pathway manner, with the core mechanism involving the inhibition of osteocyte apoptosis.
Keywords: Network Pharmacology; Molecular Dynamics Simulation; Panax Notoginseng Saponins; Alcohol-Induced Osteonecrosis of the Femoral Head; Machine Learning; Osteocyte Apoptosis

1 Introduction

Alcohol-induced osteonecrosis of the femoral head (AIONFH) is a common orthopedic disorder, which arises from chronic alcohol abuse and is defined by disrupted or severely compromised femoral head blood perfusion. This pathological process subsequently triggers osteocyte necrosis, femoral head structural collapse and progressive deterioration of hip joint function. Clinically, AIONFH manifests as hip or inguinal pain, while advanced cases present with limb shortening, abnormal gait and restricted hip mobility **[1-3]**. Epidemiological data indicate that AIONFH accounts for 20% – 40% of non-traumatic osteonecrosis of the femoral head, predominantly affecting long-term alcohol consumers aged 30-50 years, with an increasing trend of younger onset **[4]**. Currently, statins and anticoagulants are the mainstay of hip-preserving therapy for AIONFH, but their therapeutic efficacy is suboptimal, and the majority of patients eventually require total hip arthroplasty **[5]**. Hence, it is imperative to develop novel and effective intervention strategies for AIONFH via experimental investigation.

Panax Notoginseng Saponins (PNS), the major bioactive constituents extracted from the rhizome of Panax notoginseng (a classic traditional Chinese medicine), are renowned for their pro-angiogenic, anti-inflammatory and anticoagulant properties. PNS has been extensively applied in the clinical management of cardiovascular, cerebrovascular and bone loss disorders **[6,7]**. Furthermore, accumulating evidence

confirms that PNS can effectively enhance bone microcirculation and suppress osteocyte apoptosis **[8]**. In vitro studies have demonstrated that PNS markedly elevates intraosseous capillary density, reduces bone marrow adipogenesis and lowers osteocyte mortality via activating the PI3K/Akt signaling pathway **[9]**. Existing research also indicates that PNS mitigates femoral head collapse by upregulating the expression of angiogenic and osteogenic proteins **[10]**. Collectively, PNS represents a promising therapeutic candidate for AIONFH.

Despite its well-documented anti-inflammatory, pro-angiogenic and bone regenerative activities, the precise molecular mechanism underlying the therapeutic effects of PNS against AIONFH remains incompletely understood **[11-15]**. In recent years, computational approaches, including network pharmacology, molecular docking and multi-dimensional bioinformatics analysis, have been widely adopted to unravel the pharmacological mechanisms of drugs in disease treatment, enabling the elucidation of disease pathogenesis and drug intervention pathways **[16-19]**.

This study aimed to systematically clarify the therapeutic potential of PNS for AIONFH, identify its key therapeutic targets and uncover the underlying molecular mechanisms via integrating network pharmacology, molecular docking and molecular dynamics simulation. Additionally, in vivo experiments in rats were performed to further validate the therapeutic efficacy of PNS against AIONFH and empirically explore the associated pharmacological mechanisms. The findings of this study provide a robust theoretical and experimental foundation for the further development and clinical application of PNS in AIONFH treatment.

2 Methods

2.1 Network Pharmacology

2.1.1 Acquisition of PNS Active Components and Corresponding Targets

The major active components of PNS and their canonical SMILES structures were retrieved from the Traditional Chinese Medicine Systems Pharmacology Database and Analysis Platform (TCMSP, https://old.tcmsp-e.com/tcmsp.php). PubChem Database (https://pubchem.ncbi.nlm.nih.gov/) and peer-reviewed literature. Target prediction for each active component was conducted using PharmMapper (https://www.lilab-ecust.cn/pharmmapper/index.html). The PNS target dataset was constructed after data integration and redundancy removal.

2.1.2 Acquisition of Disease-Related Targets

Using the keywords “Alcohol-induced Osteonecrosis of the Femoral Head” and “AIONFH”, AIONFH-associated target genes were collected from the GeneCards Database (https://www.genecards.org/), Online Mendelian Inheritance in Man (OMIM, https://www.omim.org/), DisGeNET Database (https://www.disgenet.org/) and Therapeutic Target Database (TTD, http://db.idrblab.net/ttd/). All retrieved targets were merged and deduplicated to establish the AIONFH target dataset.

2.1.3 Screening of Drug-Disease Common Targets

A Venn diagram of drug-disease targets was generated using the Jvenn online tool (http://www.bioinformatics.com.cn/static/others/jvenn/example.html) to identify overlapping targets, which were defined as potential therapeutic targets of PNS for AIONFH and subjected to subsequent analyses. The PNS active components and overlapping targets were imported into Cytoscape 3.9.1 for visualization, constructing a drug-active component-target network.

2.1.4 Construction and Analysis of Protein-Protein Interaction (PPI) Network

The overlapping targets were uploaded to the STRING database (https://string-db.org/), with the species restricted to Homo sapiens and an interaction confidence score threshold of $\geqslant 0.4$, to acquire PPI network data. The resulting TSV file was imported into Cytoscape 3.9.1 for further visualization and topological analysis of the PPI network.

2.1.5 GO Functional Enrichment and KEGG Pathway Enrichment Analysis

GO functional enrichment and KEGG pathway enrichment analyses of the overlapping targets were performed using R software. GO analysis comprised three categories: Biological Process (BP), Cellular Component (CC) and Molecular Function (MF). A significance threshold of $P < 0.05$ was applied, and GO bar plots and KEGG bubble plots were generated accordingly.

2.1.6 Screening of Core Targets by Machine Learning Based on GEO Database

The GEO dataset GSE74089 was selected as the analytical matrix to screen core targets from the overlapping targets using three independent machine learning algorithms. Logistic regression was performed via the glmnet package in R, with three-fold cross-validation for feature selection and variable importance evaluated based on coefficient magnitudes. Support Vector Machine-Recursive Feature Elimination (SVM-RFE) was applied to integrate SVM and RFE for optimal variable combination screening. Random Forest models were constructed using the randomForest package in R, and feature importance rankings were generated via cross-validation for target prioritization. Targets commonly identified by all three algorithms were defined as the final core therapeutic targets for subsequent investigations.

2.2 Molecular Docking

Two-dimensional (2D) structures of PNS active components were retrieved from the PubChem Database (http://pubchem.ncbi.nlm.nih.gov/), and three-dimensional (3D) structures were generated using ChemOffice software and saved as mol2 files. High-resolution crystal structures of core target proteins were downloaded from the RCSB Protein Data Bank (RCSB PDB, http://www.rcsb.org/). Protein structures were processed (dehydration and dephosphorylation) using PyMOL 2.6 and saved as PDB files. Protein and ligand structures were further preprocessed using AutoDock 1.5.6,

including protein hydrogenation/dehydration, ligand hydrogenation and torsion angle optimization, followed by docking box coordinate determination. Molecular docking was performed using AutoDock Vina to evaluate protein-ligand interactions. The optimal binding conformation was selected based on docking scores. Molecular docking results were visualized using Discovery Studio 2019 and PyMOL 2.6, generating 2D and 3D interaction diagrams between compounds and key amino acid residues.

2.3 Molecular Dynamics

Molecular dynamics simulation was conducted using GROMACS 2023.2. Ligand parameterization was performed using the GAFF force field in AmberTools22, and RESP charges were calculated via Gaussian 16w after ligand hydrogenation. The protein was described using the Amber99sb-ildn force field. The simulation system was solvated with the TIP3P water model, neutralized with sodium ions, and simulated at 300 K and 1 bar **[20]**. The system was initially subjected to energy minimization via the steepest descent method (maximum 50,000 steps). Sequential equilibration was performed in the NVT (isothermal-isochoric) and NPT (isothermal-isobaric) ensembles (100,000 steps each, 1 fs/step, 100 ps total). Temperature coupling was achieved via the V-rescale algorithm, and pressure coupling in the NPT ensemble used the Parrinello-Rahman method. A 100 ns production run (50,000,000 steps, 2 fs/step) was then performed. Post-simulation trajectory analysis was conducted using GROMACS built-in tools, calculating root mean square deviation (RMSD), root mean square fluctuation (RMSF), radius of gyration (Rg) and solvent accessible surface area (SASA). Binding free energy was calculated using the gmx_MMPBSA tool based on the MM/GBSA method, and residue energy decomposition analysis was performed using the GB solvation model.

2.4 Animal Experiment Verification

2.4.1 Animal Preparation

Forty-eight specific pathogen-free (SPF) male Sprague-Dawley (SD) rats (200 ± 20 g) were purchased from Changsha Tianqin Biotechnology Co., Ltd. (Production License: SCXK (Xiang) 2019-0014; Use License: SYXK (Gui) 2022-0001). Rats were housed in a controlled environment (20–25° C, 50%–65% relative humidity, 12 h light/dark cycle) with ad libitum access to standard chow and water. All animal experiments were performed in accordance with the 3R principles (Replacement, Reduction, Refinement) and approved by the Animal Experimental Ethics Committee of Guangxi Zhuang Autonomous Region Academy of Chinese Medical Sciences (Approval No.: 2024093001).

Clinical trial registration: Not applicable.

2.4.2 Experimental Operations

2.4.2.1 Experimental Grouping and Model Establishment

After 7 days of acclimatization, 48 SPF male SD rats were randomly assigned to six groups (n=8 per group) using a random number table: normal control (NC), AIONFH

model, compound ossotide positive control (PC), low-dose PNS, medium-dose PNS and high-dose PNS. Except for the NC group, rats in the other groups were intragastrically administered 46% ethanol (10 mL/kg) daily for 45 consecutive days to establish the AIONFH model. After modeling, two rats from the model group were randomly selected for model validation. Rats were euthanized via excessive pentobarbital sodium (China National Pharmaceutical Group Shanghai Chemical Reagent Co., Ltd., Batch No.: F20020915) anesthesia. The left femoral head was rapidly harvested, fixed in 4% paraformaldehyde for 48 h, and subjected to micro-computed tomography (micro-CT) to confirm successful AIONFH model establishment.

2.4.2.2 Drug Intervention and Sample Collection

Following successful model validation, drug intervention was initiated while maintaining ethanol administration. Rats in the NC and model groups received intraperitoneal injection of normal saline (0.2 mL/kg/day). The PC group was administered compound ossotide injection (27.0 mg/mL, 0.2 mL/kg/day; Hebei Zhitong Biopharmaceutical Co., Ltd., National Medicine Approval No. H20052314, Batch No. 0240402). The low-, medium- and high-dose PNS groups received PNS injection (0.2 mL/kg/day; Beijing Puxitang Biotechnology Co., Ltd., Batch No. C24PA120A) at concentrations of 67.5 mg/mL, 135.0 mg/mL and 270.0 mg/mL, respectively. All interventions were administered daily for 45 consecutive days. Rats were fasted for 12 h (with free access to water) after the last administration, anesthetized via intraperitoneal pentobarbital sodium (40 mg/kg), and sacrificed. Blood was collected from the abdominal aorta, and bilateral femoral heads were harvested for subsequent analyses.

2.4.3 Pathological Staining Analysis of Femoral Head

Left femoral heads from each group were decalcified using EDTA solution (replaced every 3 days), with decalcification endpoint defined as easy penetration by an acupuncture needle. Tissues were routinely embedded in paraffin and sectioned at 4 μm. Tartrate-resistant acid phosphatase (TRAP) staining (Shanghai Gefan Biotechnology Co., Ltd., Cat. No.: M071, Batch No.: 20250317), hematoxylin-eosin (HE) staining (Beijing Leagene Biotechnology Co., Ltd., Batch No.: 0509A22), Alizarin Red staining (Shanghai Gefan Biotechnology Co., Ltd., Cat. No.: M040, Batch No.: 20250317) and alkaline phosphatase (ALP) staining (Shanghai Gefan Biotechnology Co., Ltd., Cat. No.: M039, Batch No.: 20250317) were performed to evaluate femoral head pathological changes.

2.4.4 Detection of Target Protein Expression Localization and Level by Immunofluorescence Staining

Paraffin sections of right femoral head tissues were dewaxed and subjected to routine immunofluorescence staining. The localization and expression of HSD11B1 protein (1:500) were observed under a fluorescence microscope, and images were captured for analysis.

2.4.5 Detection of Target Gene Expression by qPCR

Total RNA was extracted from right femoral head tissues using the TRIzol method and reverse-transcribed into complementary DNA (cDNA). The mRNA expression levels of Runx2, CTSK and HSD11B1 were quantified via qPCR. Primer sequences and qPCR conditions are listed in Table 1.

[Table 1 near here]

2.4.6 Statistical Methods

All experimental data are presented as mean ± standard deviation (SD) and analyzed using SPSS 16.0 software. Data normality was confirmed via normality tests. Multiple group comparisons were performed using one-way analysis of variance (ANOVA). Pairwise comparisons were conducted using the Bonferroni test for homogeneous variances and Tamhane's T2 test for heterogeneous variances. Statistical significance was defined as $P < 0.05$. Significance annotations: *$P < 0.05$, **$P < 0.01$, ***$P < 0.001$, ****$P < 0.0001$, ns: no significant difference ($P \geqslant 0.05$).

3 Results

3.1 Network Pharmacology

3.1.1 PNS Active Components and Corresponding Targets

Based on the TCMSP and SwissTargetPrediction databases, combined with published literature, potential targets associated with PNS active components were screened. Five major active components were identified: Notoginsenoside R1 (NG-R1), Ginsenoside Rb1 (G-Rb1), Ginsenoside Rg1 (G-Rg1), Ginsenoside Re (G-Re) and Ginsenoside Rd (G-Rd). After data integration and redundancy removal, 127 potential PNS targets were ultimately obtained **[21-24]**.

3.1.2 AIONFH Target Set and Its Intersection Targets with PNS

AIONFH-related targets were retrieved from GeneCards, OMIM, DisGeNET and TTD databases. All entries were merged and deduplicated to establish an AIONFH target set containing 672 unique genes. As shown in Figure 1A, overlapping targets between PNS and AIONFH were identified via the Jvenn platform, generating a Venn diagram with 18 common targets. PNS active components and overlapping targets were imported into Cytoscape 3.9.1, constructing a PNS-AIONFH drug-component-target network (Figure 1B).

[Figure 1 near here]

3.1.3 Construction of PPI Network for 18 Intersection Targets

As shown in Figure 2A, the 18 overlapping targets were submitted to the STRING database to construct a PPI network (18 nodes, 55 edges; average node degree = 6.11). The F2 gene was excluded due to its isolation from the main network. The optimized PPI network contained 17 nodes and 55 edges (Figure 2B), visualized via Cytoscape 3.9.1.

[Figure 2 near here]

3.1.4 GO Enrichment Analysis and KEGG Pathway Enrichment Analysis

GO functional enrichment and KEGG pathway enrichment analyses of the 18 overlapping targets were performed using R software ($P < 0.05$). GO analysis identified 1042 significant Biological Process (BP), 14 Cellular Component (CC) and 109 Molecular Function (MF) terms (Figure 3A). KEGG analysis revealed 38 significantly enriched pathways; the top 10 pathways (ranked by P value) are presented in a bubble plot (Figure 3B).

[Figure 3 near here]

3.1.5 Screening of Core Targets by Machine Learning Based on GEO Database

To identify core therapeutic targets, the GEO dataset GSE74089 was analyzed using three machine learning algorithms: logistic regression, SVM-RFE and random forest. Targets commonly identified by all three algorithms were defined as core targets (Figure 4A). Six core genes were obtained: FGF2, HSD11B1, BMP2, MMP13, TYMS and VEGFA. Boxplots revealed significant differential expression of these six genes between AIONFH and control samples in GSE74089 (Figure 4B). Feature importance distributions of the three algorithms are shown in Figure 4C, while cross-algorithm importance and ranking attenuation are visualized via line charts (Figure 4D) and heatmaps (Figure 4E).

[Figure 4 near here]

3.2 Molecular Docking

Molecular docking was performed to evaluate interactions between PNS active components and the six core targets (FGF2, HSD11B1, BMP2, MMP13, TYMS, VEGFA). Five PNS components (NG-R1, G-Rb1, G-Rg1, G-Re, G-Rd) were docked with each target. Docking results are summarized in Table 2, visualized as a heatmap (Figure 5), and the top six binding pairs are shown in Figure 6. All complexes exhibited binding energies < -5.0 kcal/mol, indicating potential binding activity; energies < -7.0 kcal/mol reflect strong affinity **[25]**. Ginsenoside Re showed the strongest affinity for HSD11B1 ($\Delta G = -12.4$ kcal/mol).

[Figure 5 near here]

[Table 2 near here]

[Figure 6 near here]

3.3 Molecular Dynamics

Given the strongest binding between HSD11B1 and G-Re, 100 ns molecular dynamics simulation was performed on the G-Re – HSD11B1 complex (Figure 7).

Root mean square deviation (RMSD) assesses conformational stability, with values of 0.1 – 0.5 nm indicating a stable system **[26]**. The G-Re – HSD11B1 complex

maintained RMSD < 0.4 Å throughout the 100 ns simulation (fluctuation < 0.05 Å; Figure 7A). The receptor and complex RMSD curves overlapped closely without upward drift, confirming no major conformational rearrangement, high thermodynamic stability, and stable ligand positioning in the binding pocket.

Radius of gyration (Rg) reflects protein structural compactness **[26]**. The complex Rg remained at 2.64 – 2.76 Å (fluctuation < 0.05 Å; Figure 7B), with no significant trend, indicating no structural loosening or overfolding and a stably compact protein backbone.

Root mean square fluctuation (RMSF) measures residue flexibility: low values indicate stable core regions, high values indicate flexible loops/termini **[26]**. Most residues in the complex had RMSF < 0.4 Å; only a few terminal residues showed slightly higher fluctuations (max < 0.6 Å; Figure 7C). Ligand binding did not disrupt core rigidity, and the binding pocket remained conformationally stable for sustained interaction.

Solvent-accessible surface area (SASA) quantifies solvent-exposed surface and reflects binding pocket microenvironment changes **[26]**. Complex SASA remained at 276 – 304 arbitrary units (fluctuation < 5%; Figure 7D), with no significant trend. G-Re binding did not alter surface hydrophobic exposure or disrupt pocket microenvironment, ensuring complex thermodynamic stability.

Hydrogen bonds are critical for complex stability and binding affinity **[26]**. The number of hydrogen bonds between G-Re and HSD11B1 remained stable at 2 – 3 throughout the simulation (Figure 7E), with no sustained decrease. G-Re formed persistent hydrogen bonds with pocket residues (e.g., ALA172, ILE46), consistent with docking results and supporting stable binding.

Residue free energy decomposition (MM/GBSA) identifies key binding residues: negative values indicate favorable contributions **[27,28]**. Fifteen residues contributed negatively to binding (Figure 7F, Table 3). ASP323 was the dominant contributor (−2.679), followed by ALA212 (−1.72), GLU353 (−1.568) and LYS211 (−1.559). Residues such as PHE227 (−0.197) and THR231 (−0.243) had minor contributions. Binding relied on coordinated hydrogen bonds, electrostatic and hydrophobic interactions at key residues, defining the molecular basis of G-Re – HSD11B1 specificity.

Collectively, molecular dynamics confirmed that the G-Re – HSD11B1 complex exhibits high conformational stability and binding specificity. Low fluctuations in RMSD, Rg and SASA, stable hydrogen bonds and favorable residue contributions collectively ensure persistent specific binding. These findings provide reliable microdynamic evidence that PNS acts via G-Re to target and inhibit HSD11B1, thereby improving the AIONFH bone marrow microenvironment.

[Figure 7 near here]

[Table 3 near here]

3.4 Animal Experiment Verification

3.4.1 Results of Femoral Head Pathological Staining

TRAP, HE, Alizarin Red and ALP staining were performed to evaluate PNS effects on bone metabolism in AIONFH (Figure 8).

TRAP staining (×100): NC rats showed physiological osteoclast distribution and activity **[29]**. The AIONFH model exhibited excessive osteoclast activation and enhanced bone resorption. PNS treatment dose-dependently suppressed osteoclast overactivity; the high-dose group resembled NC, indicating PNS regulates bone resorption balance.

HE staining (×100): NC rats had intact bone structure, orderly osteocytes/trabeculae and normal marrow adipocytes **[30]**. The AIONFH model showed sparse/fractured trabeculae, adipocyte hyperplasia, disorganized osteocytes and increased empty lacunae. PNS intervention dose - dependently repaired trabecular morphology, restricted adipocyte proliferation and restored structure; medium/high-dose groups approached NC, confirming PNS promotes bone repair and optimizes the marrow microenvironment.

Alizarin Red staining (×100): NC rats showed uniform calcium deposition **[31]**. The AIONFH model exhibited reduced deposition and impaired mineralization. PNS dose-dependently enhanced calcium deposition; the high - dose group was near NC, demonstrating PNS promotes mineralization and restores calcium homeostasis.

ALP staining (×100): NC rats had normal osteoblast activity and strong positive staining **[32]**. The AIONFH model showed suppressed osteoblast activity. PNS dose-dependently increased osteoblast activity; the high-dose group had robust staining and restored osteogenesis, verifying PNS activates osteoblasts and enhances bone formation.

[Figure 8 near here]

3.4.2 Immunofluorescence Staining of HSD11B1 Protein

Immunofluorescence staining (Figure 9): HSD11B1 localized primarily in the femoral head cytoplasm (green fluorescence; DAPI: blue nuclei). NC rats showed weak HSD11B1 fluorescence. The AIONFH model had significantly increased intensity. PNS treatment dose-dependently reduced HSD11B1 fluorescence. Thus, HSD11B1 is upregulated in AIONFH, and PNS suppresses its overexpression in a dose-dependent manner.

[Figure 9 near here]

3.5 Results of HSD11B1, Runx2 and CTSK Gene Expression Detected by qPCR

qPCR results (Figure 10): HSD11B1: Significantly upregulated in AIONFH vs NC. PC and medium/high-dose PNS significantly downregulated HSD11B1 (****P < 0.0001); low-dose PNS had no effect (ns); Runx2: Suppressed in AIONFH. PC and medium/high-dose PNS significantly restored Runx2 (****P < 0.0001); low-dose PNS had no effect (ns). Runx2 is a master osteogenic transcription factor **[33]**; CTSK: Elevated in AIONFH. PC and PNS groups showed a trend toward reduced CTSK, but differences were not significant (ns). CTSK is a key osteoclast effector **[34]**.

Collectively, AIONFH rats exhibited abnormal upregulation of HSD11B1/CTSK and downregulation of Runx2. PNS dose-dependently reversed HSD11B1 and Runx2 dysregulation (significant at medium/high doses), while CTSK reduction was non-significant. PNS likely restores osteoblast-osteoclast balance via HSD11B1 inhibition and Runx2 activation, mediating therapeutic effects in AIONFH.

[Figure 10 near here]

4 Discussion

This study integrated network pharmacology, machine learning, molecular docking, molecular dynamics simulation and in vivo experiments to systematically elucidate the core mechanism of PNS against AIONFH from a component-target-pathway-phenotype multi-dimensional perspective, providing a scientific basis for clinical translation.

AIONFH arises from chronic alcohol exposure, leading to femoral head ischemia, osteocyte apoptosis and bone matrix destruction **[35]**. Alcohol upregulates HSD11B1, driving conversion of inactive corticosterone to active cortisol, promoting marrow adipogenesis and compressing intraosseous capillaries **[36,37]**. Concurrently, alcohol suppresses angiogenic factors (VEGFA, FGF2), establishing an ischemia - osteonecrosis vicious cycle **[38-41]**. Alcohol also activates MMP13-mediated matrix degradation and dysregulates BMP2 - dependent osteoblast differentiation, compromising bone structural stability **[42-45]**. Here, 18 common targets were identified between PNS and AIONFH. GO enrichment highlighted involvement in osteoblast differentiation, consistent with AIONFH pathogenesis. KEGG analysis prioritized the VEGF pathway as critical, regulating endothelial proliferation/lumen formation to improve the ischemic microenvironment. Three machine learning algorithms (logistic regression, SVM-RFE, random forest) further refined six core targets: FGF2, HSD11B1, BMP2, MMP13, TYMS and VEGFA, enhancing target reliability and clinical relevance.

Molecular docking validates component-target binding specificity. All five PNS components docked to six core targets with $\Delta G < -5.0$ kcal/mol (potential activity). Ginsenoside Re bound HSD11B1 with the highest affinity ($\Delta G = -12.4$ kcal/mol; strong affinity threshold < -7.0 kcal/mol), representing a key molecular interaction. A 100 ns molecular dynamics simulation confirmed complex stability: RMSD < 0.04

nm (minimal fluctuation), Rg = 2.64 – 2.76 Å (stable compactness), SASA fluctuation < 5% and persistent 2 – 3 hydrogen bonds. No ligand drift occurred in the binding pocket. Residue decomposition identified ASP323 and ALA212 as critical for stable binding, defining the atomic-level mechanism of PNS targeting HSD11B1.

In vivo experiments are the gold standard for therapeutic validation. Here, an AIONFH rat model confirmed dose-dependent PNS efficacy via multi-faceted bone metabolism analyses. HE staining showed PNS repairs trabecular damage, reduces adipocyte hyperplasia, lowers empty lacunae and restores femoral head integrity. TRAP staining confirmed PNS suppresses osteoclast overactivation and reverses excessive bone resorption. ALP staining verified enhanced calcium deposition, osteoblast activity and mineralization, restoring bone formation-resorption balance. Mechanistically, immunofluorescence and qPCR confirmed PNS dose-dependently suppresses HSD11B1 (protein/mRNA) and restores Runx2 expression in AIONFH femoral heads. HSD11B1 is a critical regulator of local glucocorticoid metabolism, converting inactive 11 - dehydrocorticosterone to active corticosterone; its overexpression is a key AIONFH driver **[46]**. Excessive HSD11B1 increases local active glucocorticoids, driving marrow mesenchymal stem cell adipogenesis, capillary compression, ischemia, osteoblast inhibition and osteoclast activation—ultimately causing trabecular destruction, osteocyte apoptosis and structural collapse. Integrating docking and dynamics data, PNS acts primarily via G-Re binding to HSD11B1 and inhibiting its activity. This reduces local glucocorticoid overproduction, relieves vascular compression, synergistically activates VEGF/FGF2-mediated angiogenesis, restores blood flow and breaks the ischemia-osteonecrosis cycle. PNS achieves multi-link therapeutic effects: improved perfusion, balanced bone metabolism and inhibited osteocyte apoptosis, enabling targeted AIONFH treatment.

5 Innovations and Limitations of This Study

This study established a rigorous in silico prediction → molecular validation → in vivo verification research chain. Network pharmacology combined with machine learning enabled unbiased core target identification, avoiding limitations of traditional blind screening. Molecular docking and dynamics elucidated atomic-level component -target interactions, providing microscopic evidence for PNS pharmacology. In vivo experiments validated efficacy at pathological and molecular levels, ensuring conclusion reliability. Notably, HSD11B1 was identified as the key PNS target in AIONFH for the first time, offering a novel precision therapeutic direction.

Several limitations should be acknowledged. Network pharmacology screening relied on existing databases, potentially missing low-abundance components or unannotated targets. Molecular dynamics was limited to the G-Re – HSD11B1 complex, not covering all core pairs, thus incomplete representation of multi-target synergy. The AIONFH model did not recapitulate clinical comorbidities (e.g., liver injury, metabolic syndrome). Intervention duration was short, and long-term effects on femoral head structural stability were not assessed.

Future work will use CRISPR/Cas9 knockout to validate core target necessity. PNS monomers will be isolated to assess individual effects and multi-component synergy mechanisms. Clinically relevant composite AIONFH models will be developed for long-term interventions and small-sample clinical studies to further validate PNS efficacy and safety.

6 Conclusion

This multi-dimensional study demonstrates that PNS treats AIONFH via multi-component, multi-target and multi-pathway mechanisms. Active components (NG-R1, G-Rg1, G-Re) bind core targets (FGF2, HSD11B1, VEGFA) and activate the VEGF pathway, exerting multi-link benefits: improved perfusion, inhibited osteocyte apoptosis and balanced bone metabolism. Ginsenoside Re–HSD11B1 binding and glucocorticoid inhibition represent the key molecular mechanism underlying PNS-mediated marrow microenvironment improvement. This work provides robust experimental evidence for PNS as a promising AIONFH therapy and establishes a computational-experimental integrated paradigm for dissecting multi-component/multi-target mechanisms of traditional Chinese medicines. It advances TCM modernization and informs novel therapeutic strategies for orthopedic diseases.

List of abbreviations

Alcohol-induced osteonecrosis of the femoral head (AIONFH)
Panax Notoginseng Saponins (PNS)
Notoginsenoside R1 (NG-R1)
Ginsenoside Rb1 (G-Rb1)
Ginsenoside Rg1 (G-Rg1)
Ginsenoside Re (G-Re)
Ginsenoside Rd (G-Rd)
Gene Expression Omnibus (GEO)
Hematoxylin-eosin (HE)
Tartrate-resistant acid phosphatase (TRAP)
Alizarin Red and alkaline phosphatase (AKP)
the Root Mean Square Deviation (RMSD)
Root Mean Square Fluctuation (RMSF)
Radius of Gyration (Rg)
Solvent Accessible Surface Area (SASA)
quantitative real-time polymerase chain reaction (qPCR)
11 β -hydroxysteroid dehydrogenase type 1 (HSD11B1)
vascular endothelial growth factor A (VEGFA)
fibroblast growth factor 2 (FGF2)
matrix metalloproteinase 13 (MMP13)
bone morphogenetic protein 2 (BMP2)
Kyoto Encyclopedia of Genes and Genomes (KEGG)
Biological Process (BP)
Cellular Component (CC)
Molecular Function (MF)
upport vector machine-recursive feature elimination (SVM-RFE)
thymidylate synthase (TYMS)
Runt-related transcription factor 2 (Runx2)
analysis of variance (ANOVA)
Generalized Born (GB)

Declarations

Ethics approval and consent to participate
The Animal Experimental Ethics Committee Approval No. of Guangxi Zhuang Autonomous Region Academy of Chinese Medical Sciences was 2024093001. Clinical trial number: not applicable.

Consent for publication
Not applicable

Availability of data and materials
All data generated or analysed during this study are included in this published article [and its supplementary information files].

Competing interests
The authors declare no competing financial or non-financial interests. The funders had no role in the design or conduct of this study.

Funding
This study was supported by the Guangxi Natural Science Foundation Project (General Program, Grant No.: 2024GXNSFAA010370) and the Guangxi Traditional Chinese Medicine Appropriate Technology Development and Promotion Project (Grant No.: GZSY2026008).

Authors' contributions
Bai R:wrote the main manuscript text
Shu H: prepared figures
Mo J:provided funding
Zhang X:reviewed the manuscript
Li Z:reviewed the manuscript
Chen X:reviewed the manuscript
Ye S:reviewed the manuscript
Nie X:reviewed the manuscript
Chen S:reviewed the manuscript
Liang B:provided funding

Acknowledgements
This work was supported by the Guangxi Natural Science Foundation (Grant No. 2024GXNSFAA010370) and the Guangxi Traditional Chinese Medicine Appropriate Technology Development and Promotion Project (Grant No. GZSY2026008). The authors thank the supporting institutions and the Animal Experimental Ethics Committee of Guangxi Zhuang Autonomous Region Academy of Chinese Medical Sciences for ethical approval.

References

[1] Chen, Wei et al. Zhongguo xiu fu chong jian wai ke za zhi = Zhongguo xiufu chongjian waike zazhi = Chinese journal of reparative and reconstructive surgery vol. 36,11 (2022): 1420-1427. doi:10.7507/1002-1892.202206072

[2] Li, Zilin et al. “Advances in experimental models of osteonecrosis of the femoral head.” Journal of orthopaedic translation vol. 39 88-99. 3 Feb. 2023, doi:10.1016/j.jot.2023.01.003

[3] Kumar, Prasoon et al. “Association of Specific Genetic Polymorphisms with Atraumatic Osteonecrosis of the Femoral Head: A Narrative Review.” Indian journal of orthopaedics vol. 56,5 771-784. 6 Jan. 2022, doi:10.1007/s43465-021-00583-3

[4] Lou, Yuhan et al. “Etiology, pathology, and treatment of osteonecrosis of the femoral head in adolescents: A comprehensive review.” Medicine vol. 103,30 (2024): e39102. doi:10.1097/MD.0000000000039102

[5] Zhu, Weihong et al. “Bioengineering strategies targeting angiogenesis: Innovative solutions for osteonecrosis of the femoral head.” Journal of tissue engineering vol. 16 20417314241310541. 24 Jan. 2025, doi:10.1177/20417314241310541

[6] Chen, Xu et al. “Exploring the protective effects of PNS on acute myocardial ischaemia-induced heart failure by Transcriptome analysis.” Journal of ethnopharmacology vol. 271 (2021): 113823. doi:10.1016/j.jep.2021.113823

[7] Fan, Jing-Zheng et al. “Panax notoginseng saponins mitigate ovariectomy-induced bone loss and inhibit marrow adiposity in rats.” Menopause (New York, N.Y.) vol. 22,12 (2015): 1343-50. doi:10.1097/GME.0000000000000471

[8] Yuan, Heng-Feng et al. “Protective effects of total saponins of panax notoginseng on steroid-induced avascular necrosis of the femoral head in vivo and in vitro.” Evidence-based complementary and alternative medicine : eCAM vol. 2015 (2015): 165679. doi:10.1155/2015/165679

[9] Yang, Wen-Jing et al. Zhongguo Zhong yao za zhi = Zhongguo zhongyao zazhi = China journal of Chinese materia medica vol. 48,4 (2023): 1087-1097. doi:10.19540/j.cnki.cjcmm.20220926.501

[10] Feng, Guiyu et al. “Sequential Release of Panax Notoginseng Saponins and Osteopractic Total Flavone from Poly (L-Lactic Acid) Scaffold for Treating Glucocorticoid-Associated Osteonecrosis of Femoral Head.” Journal of functional biomaterials vol. 14,1 31. 4 Jan. 2023, doi:10.3390/jfb14010031

[11] Qu, Jing et al. “Panax notoginseng saponins and their applications in nervous system disorders: a narrative review.” Annals of translational medicine vol. 8,22 (2020): 1525. doi:10.21037/atm-20-6909

[12] Xiao, Haiyan et al. “Panax notoginseng saponins promotes angiogenesis after cerebral ischemia-reperfusion injury.” Journal of ginseng research vol. 48,6 (2024): 592-602. doi:10.1016/j.jgr.2024.08.004

[13] Sun, Tao et al. “Effect of Panax notoginseng Saponins on Focal Cerebral Ischemia-Reperfusion in Rat Models: A Meta-Analysis.” Frontiers in pharmacology vol. 11 572304. 9 Feb. 2021, doi:10.3389/fphar.2020.572304

[14] Liu, Lu et al. “Effects of Panax notoginseng saponins on alleviating low shear induced

endothelial inflammation and thrombosis via Piezo1 signalling." Journal of ethnopharmacology vol. 335 (2024): 118639. doi:10.1016/j.jep.2024.118639
[15] Wei, Chen Chao et al. "Panax notoginseng saponins alleviate osteoporosis and joint destruction in rabbits with antigen-induced arthritis." Experimental and therapeutic medicine vol. 22,5 (2021): 1302. doi:10.3892/etm.2021.10737
[16] Zhang, Peng et al. "Network pharmacology: towards the artificial intelligence-based precision traditional Chinese medicine." Briefings in bioinformatics vol. 25,1 (2023): bbad518. doi:10.1093/bib/bbad518
[17] Li, Shao et al. Zhongguo Zhong yao za zhi = Zhongguo zhongyao zazhi = China journal of Chinese materia medica vol. 48,22 (2023): 5965-5976. doi:10.19540/j.cnki.cjcmm.20230923.701
[18] Zhou, Meng-Nan et al. Zhongguo Zhong yao za zhi = Zhongguo zhongyao zazhi = China journal of Chinese materia medica vol. 46,9 (2021): 2363-2369. doi:10.19540/j.cnki.cjcmm.20210222.201
[19] Yang, Xulong et al. "Treatment of liver fibrosis in hepatolenticular degeneration with traditional Chinese medicine: systematic review of meta-analysis, network pharmacology and molecular dynamics simulation." Frontiers in medicine vol. 10 1193132. 11 May. 2023, doi:10.3389/fmed.2023.1193132
[20] Harrach, Michael F, and Barbara Drossel. "Structure and dynamics of TIP3P, TIP4P, and TIP5P water near smooth and atomistic walls of different hydroaffinity." The Journal of chemical physics vol. 140,17 (2014): 174501. doi:10.1063/1.4872239
[21] Yao, Chang-liang et al. "Simultaneous quantitation of five Panax notoginseng saponins by multi heart-cutting two-dimensional liquid chromatography: Method development and application to the quality control of eight Notoginseng containing Chinese patent medicines." Journal of chromatography. A vol. 1402 (2015): 71-81. doi:10.1016/j.chroma.2015.05.015
[22] Yang, Xiaochen et al. "Protective effects of panax notoginseng saponins on cardiovascular diseases: a comprehensive overview of experimental studies." Evidence-based complementary and alternative medicine : eCAM vol. 2014 (2014): 204840. doi:10.1155/2014/204840
[23] Zhou, Ping et al. "Ginsenoside Rb1 and mitochondria: A short review of the literature." Molecular and cellular probes vol. 43 (2019): 1-5. doi:10.1016/j.mcp.2018.12.001
[24] Guo, Shasha et al. "Notoginsenoside R1: A systematic review of its pharmacological properties." Die Pharmazie vol. 74,11 (2019): 641-647. doi:10.1691/ph.2019.9534
[25] Yang, Chao et al. "Protein-Ligand Docking in the Machine-Learning Era." Molecules (Basel, Switzerland) vol. 27,14 4568. 18 Jul. 2022, doi:10.3390/molecules27144568
[26] Wu, Xiaodong et al. "Application of molecular dynamics simulation in biomedicine." Chemical biology & drug design vol. 99,5 (2022): 789-800. doi:10.1111/cbdd.14038
[27] Xia W, He L, Bao J, et al. Insights into small molecule inhibitor bindings to PD-L1 with residue-specific binding free energy calculation. J Biomol Struct Dyn. 2022;40(22):12277-12285.
[28] Coskun D, Chen W, Clark AJ, et al. Reliable and Accurate Prediction of Single-Residue pKa Values through Free Energy Perturbation Calculations. J Chem Theory Comput. 2022， 18(12):7193-7204.
[29] Zainal Ariffin, Shahrul Hisham et al. "Evaluation of in vitro osteoblast and osteoclast differentiation from stem cell: a systematic review of morphological assays and staining techniques." PeerJ vol. 12 e17790. 25 Jul. 2024, doi:10.7717/peerj.17790
[30] Wick, Mark R. "The hematoxylin and eosin stain in anatomic pathology-An often-neglected

focus of quality assurance in the laboratory." Seminars in diagnostic pathology vol. 36,5 (2019): 303-311. doi:10.1053/j.semdp.2019.06.003
[31] Jung, M, and R Kiesslich. "Chromoendoscopy and intravital staining techniques." Bailliere's best practice & research. Clinical gastroenterology vol. 13,1 (1999): 11-9. doi:10.1053/bega.1999.0004
[32] Maguire, G A, and H Adnan. "An immunoprecipitation assay for high molecular weight alkaline phosphatase in human serum." Annals of clinical biochemistry vol. 26 (Pt 2) (1989): 151-7. doi:10.1177/000456328902600211
[33] Komori T. Molecular Mechanism of Runx2-Dependent Bone Development. Mol Cells. 2020,43(2):168-175.
[34] Zhou R, Huang R, Xu Y, Zhang D, Gu L, Su Y, Chen X, Shi W, Sun J, Gu P, Ni N, Bi X. Exosomes derived from mucoperiosteum Krt14+Ctsk+ cells promote bone regeneration by coupling enhanced osteogenesis and angiogenesis. Biomater Sci. 2024,12(22):5753-5765.
[35] Gan, Di, and Changqing Zhang. Zhongguo xiu fu chong jian wai ke za zhi = Zhongguo xiufu chongjian waike zazhi = Chinese journal of reparative and reconstructive surgery vol. 27,3 (2013): 365-8.
[36] Ahmed, Adeeba et al. "Induction of hepatic 11beta-hydroxysteroid dehydrogenase type 1 in patients with alcoholic liver disease." Clinical endocrinology vol. 68,6 (2008): 898-903. doi:10.1111/j.1365-2265.2007.03125.x
[37] Zhu, Kai et al. "Study on the mechanism of Shuanghe decoction against steroid-induced osteonecrosis of the femoral head: insights from network pharmacology, metabolomics, and gut microbiota." Journal of orthopaedic surgery and research vol. 20,1 202. 26 Feb. 2025, doi:10.1186/s13018-025-05619-0
[38] Requena-Ocaña, Nerea et al. "Vascular Endothelial Growth Factor as a Potential Biomarker of Neuroinflammation and Frontal Cognitive Impairment in Patients with Alcohol Use Disorder." Biomedicines vol. 10,5 947. 20 Apr. 2022, doi:10.3390/biomedicines10050947
[39] Varoga, Deike et al. "Differential expression of vascular endothelial growth factor in glucocorticoid-related osteonecrosis of the femoral head." Clinical orthopaedics and related research vol. 467,12 (2009): 3273-82. doi:10.1007/s11999-009-1076-3
[40] Even-Chen, Oren et al. "FGF2 is an endogenous regulator of alcohol reward and consumption." Addiction biology vol. 27,2 (2022): e13115. doi:10.1111/adb.13115
[41] Huang, Gangyong et al. "FGF2 and FAM201A affect the development of osteonecrosis of the femoral head after femoral neck fracture." Gene vol. 652 (2018): 39-47. doi:10.1016/j.gene.2018.01.090
[42] Prystupa, Andrzej et al. "Activity of MMP1 and MMP13 and amino acid metabolism in patients with alcoholic liver cirrhosis." Medical science monitor : international medical journal of experimental and clinical research vol. 21 1008-14. 7 Apr. 2015, doi:10.12659/MSM.892312
[43] Chen, Gaoyang et al. "The expression of chondrogenesis-related and arthritis-related genes in human ONFH cartilage with different Ficat stages." PeerJ vol. 7 e6306. 16 Jan. 2019, doi:10.7717/peerj.6306
[44] Gerjevic, Lisa Nicole et al. "Alcohol Activates TGF-Beta but Inhibits BMP Receptor-Mediated Smad Signaling and Smad4 Binding to Hepcidin Promoter in the Liver." International journal of hepatology vol. 2012 (2012): 459278. doi:10.1155/2012/459278
[45] Kamiya, Nobuhiro et al. "Acute BMP2 upregulation following induction of ischemic

osteonecrosis in immature femoral head." Bone vol. 53,1 (2013): 239-47. doi:10.1016/j.bone.2012.11.023
[46] Mukangwa M, Tetsuka M et al. Progesterone modulates HSD11B1-mediated cortisol production in luteinized bovine granulosa cells. J Reprod Dev. 2023;69(4):206-213. doi:10.1262/jrd.2023-005

Figure Legends

Figure 1. Venn diagram of drug-disease targets and network diagram of drug-active ingredient-action targets for PNS and AIONFH. Panel A is the Venn diagram of drug-disease targets for Panax Notoginseng Saponins (PNS)-related genes and Alcohol-induced Osteonecrosis of the Femoral Head (AIONFH)-related genes, which clearly shows the 18 overlapping targets obtained by intersecting the potential targets of PNS and the disease-related targets of AIONFH. Panel B is the visualized network diagram of drug-active ingredient-action targets between PNS and AIONFH constructed by Cytoscape 3.9.1 software, which displays the interaction relationships among PNS, its main active ingredients and the overlapping targets of the disease.

Figure 2. Protein-protein interaction (PPI) network diagrams of the overlapping targets. Panel A is the PPI network diagram of the 18 overlapping targets constructed by the STRING database, which contains 18 nodes and 55 edges with an average node degree of 6.11. Panel B is the optimized PPI network diagram processed by Cytoscape 3.9.1 software, in which the F2 target separated from the main network is excluded, and the remaining network consists of 17 nodes and 55 edges for subsequent in-depth analysis.

Figure 3. Histogram of Gene Ontology (GO) enrichment analysis and bubble plot of Kyoto Encyclopedia of Genes and Genomes (KEGG) pathway enrichment analysis. Based on the 18 overlapping targets with the significance threshold of $p<0.05$, Panel A is the GO enrichment analysis histogram, which includes 1042 significant entries for biological processes, 14 for cellular components and 109 for molecular functions. Panel B is the KEGG pathway enrichment analysis bubble plot, in which the top 10 significant pathways are selected for plotting according to the ascending order of p values from the total 38 significant pathways obtained by the analysis.

Figure 4. Identification of core targets by machine learning algorithms. Panel A is the Venn diagram of core genes, which screens out the common targets of the three machine learning algorithms as the final core therapeutic targets for PNS in the treatment of AIONFH. Panel B is the box scatter plot of inter-group comparison of core gene expression, which shows the expression profiles of the core target genes in the GSE74089 dataset and the significant expression differences between the case group and the control group. Panel C is the histogram of the importance distribution of the three machine learning algorithms (Logistic regression, SVM-RFE, Random Forest) in the screening model. Panel D is the line chart of cross-algorithm comparison of feature importance, and Panel E is the heat map of cross-algorithm comparison of feature importance and ranking attenuation, which jointly reflect the importance of each target in different screening algorithms.

Figure 5. Heat map of molecular binding energy between PNS active ingredients

and core target proteins. This heat map shows the molecular docking binding energy values (in kcal/mol) of five main active ingredients of PNS with six core target proteins of AIONFH. The color gradient of the heat map indicates the magnitude of the absolute value of the binding energy, with redder color representing a larger absolute value of binding energy, and a lower binding energy value indicating a stronger binding affinity between the small molecule and the protein.

Figure 6. Visualization of molecular docking results between core target proteins and PNS active ingredients. This figure displays the two-dimensional visualization results of the six pairs of protein-ligand complexes with the optimal molecular docking binding energy. Panel A shows the docking result of BMP2 and Ginsenoside Rd (G-Rd); Panel B shows the docking result of HSD11B1 and Ginsenoside Re (G-Re); Panel C shows the docking result of MMP13 and Notoginsenoside R1 (NG-R1); Panel D shows the docking result of TYMS and Ginsenoside Rg1 (G-Rg1); Panel E shows the docking result of VEGFA and G-Rg1; Panel F shows the docking result of BMP2 and NG-R1, all of which clearly present the key amino acid residues involved in the binding interaction.

Figure 7. Molecular dynamics simulation results of the HSD11B1-G-Re complex within 100 ns. This figure evaluates the conformational stability of the HSD11B1-G-Re complex through multiple key indicators of molecular dynamics simulation. Panel A is the root mean square deviation (RMSD) plot reflecting the conformational offset degree of the complex relative to the initial state; Panel B is the radius of gyration (Rg) plot characterizing the structural compactness of the protein; Panel C is the root mean square fluctuation (RMSF) plot representing the flexibility of each amino acid residue of the protein; Panel D is the solvent accessible surface area (SASA) plot quantifying the surface area of the molecule exposed to the solvent; Panel E is the plot of the number of hydrogen bonds between HSD11B1 and G-Re during the simulation; Panel F is the plot of residue free energy contribution, which identifies the key amino acid residues that play a core role in the stable binding of the complex.

Figure 8. Pathological staining of femoral heads in each experimental group of rats. This figure shows the results of tartrate-resistant acid phosphatase (TRAP) staining, hematoxylin-eosin (HE) staining, Alizarin Red staining and alkaline phosphatase (AKP) staining of rat femoral heads in different groups, with the magnification of ×100 for TRAP, Alizarin Red and AKP staining, and ×50 for HE staining. The groups are labeled as Normal Control (NC), Alcohol-induced Osteonecrosis of the Femoral Head model (AIONFH), Compound Ossotide Positive Control (PC), Low-dose PNS, Medium-dose PNS and High-dose PNS, which intuitively reflect the therapeutic effect of PNS on the pathological structure of femoral heads in AIONFH rats with a dose-dependent manner.

Figure 9. Immunofluorescence staining of HSD11B1 protein in rat femoral head

tissues. This figure shows the immunofluorescence staining results of HSD11B1 protein in femoral head tissues of each experimental group (NC, AIONFH, PC, Low-dose PNS, Medium-dose PNS, High-dose PNS). DAPI staining labels the cell nucleus in blue, and HSD11B1 protein is labeled with green fluorescence, which is mainly localized in the cytoplasm. The fluorescence intensity directly reflects the expression level of HSD11B1 protein, showing the dose-dependent inhibitory effect of PNS on the abnormally high expression of HSD11B1 protein in AIONFH model rats.

Figure 10. Relative mRNA expression levels of HSD11B1, Runx2 and CTSK detected by quantitative real-time polymerase chain reaction (qPCR). This figure presents the qPCR detection results of the relative mRNA expression levels of HSD11B1, Runt-related transcription factor 2 (Runx2) and Cathepsin K (CTSK) in femoral head tissues of each group (NC, AIONFH, PC, Low-dose PNS, Medium-dose PNS, High-dose PNS). The results show the abnormal expression of the three genes in the AIONFH model group and the dose-dependent reversal effect of PNS on the abnormal gene expression, that is, inhibiting the expression of HSD11B1 and CTSK and promoting the expression of Runx2.In the figure, $P<0.001$ is marked as '****', and $P \geqslant 0.05$ is marked as 'ns'.

Table 1|qPCR Primer Sequence List

GeneName	Primer Sequence(5'→3')	reheat cycles
GAPDH-F	CAAGATGGTGAAGGTCGGTG	45
GAPDH-R	TGCCGTGGGTAGAGTCATACTG	45
Runx2-F	AGTGATTTAGGGCGCATTCCT	45
Runx2-R	GATTGTGTCTGCCTGGGATCT	45
CTSK-F	CTGTGGAAGAAGACCCACGG	45
CTSK-R	ACTTCTTCGCTGGTCATGTCT	45
HSD11B1-F	AGACCAGAAATGCTCCAGGG	45
HSD11B1-R	CTTCCTCCGACCTTGCAGTC	45

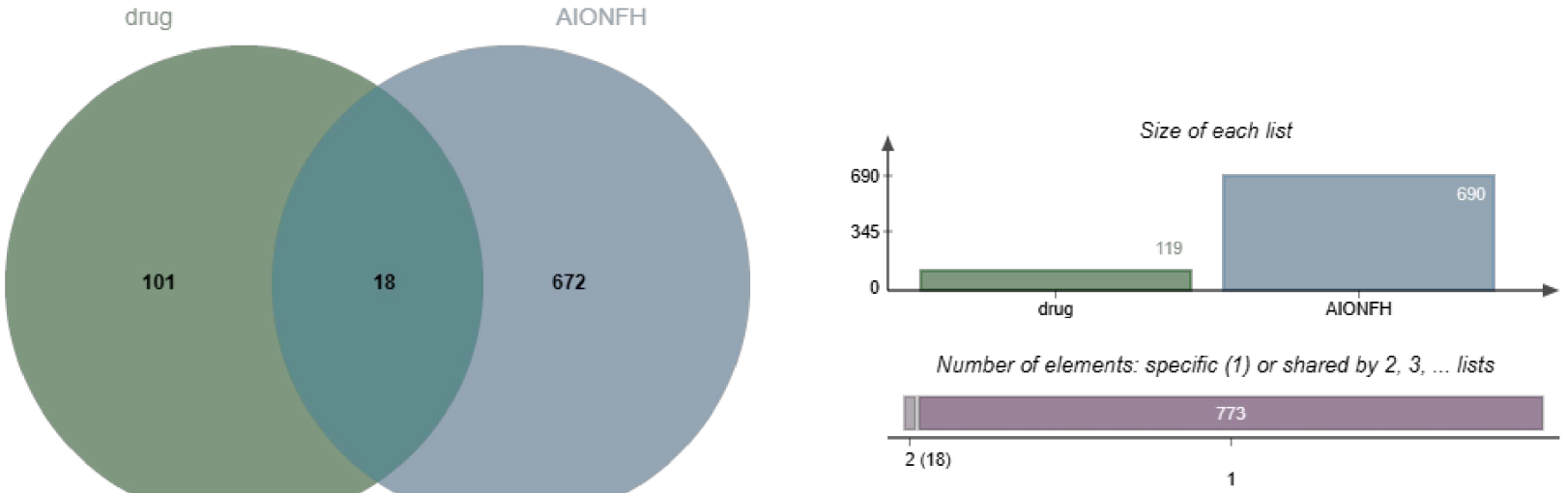
Table 2 | Molecular binding energy of PNS to target protein

Ligand	Ligand’s PubChem CID	Target	Target’s PubChem CID	Energy (kcal/mol）
NG-R1	441934	FGF2	71308511	-5.9
NG-R1	441934	HSD11B1	472407887	-6.3
NG-R1	441934	MMP13	45376872	-8.9
NG-R1	441934	TYMS	72438	-7.6
NG-R1	441934	VEGFA	505547122	-7.4
NG-R1	441934	BMP2	171361222	-8.4
G-Rb1	9898279	FGF2	71308511	-6.8
G-Rb1	9898279	HSD11B1	472407887	-8.0
G-Rb1	9898279	MMP13	45376872	-7.4
G-Rb1	9898279	TYMS	72438	-5.0
G-Rb1	9898279	VEGFA	505547122	-7.4
G-Rb1	9898279	BMP2	171361222	-7.4
G-Rg1	441923	FGF2	71308511	-6.7
G-Rg1	441923	HSD11B1	472407887	-6.2
G-Rg1	441923	MMP13	45376872	-7.9
G-Rg1	441923	TYMS	72438	-9.2
G-Rg1	441923	VEGFA	505547122	-8.1
G-Rg1	441923	BMP2	171361222	-7.4
G-Re	441921	FGF2	71308511	-6.7
G-Re	441921	HSD11B1	472407887	-12.4
G-Re	441921	MMP13	45376872	-7.6
G-Re	441921	TYMS	72438	-8.0
G-Re	441921	VEGFA	505547122	-7.8
G-Re	441921	BMP2	171361222	-7.2
G-Rd	11679800	FGF2	71308511	-7.2
G-Rd	11679800	HSD11B1	472407887	-6.6
G-Rd	11679800	MMP13	45376872	-7.7
G-Rd	11679800	TYMS	72438	-7.9
G-Rd	11679800	VEGFA	505547122	-7.9
G-Rd	11679800	BMP2	171361222	-8.7

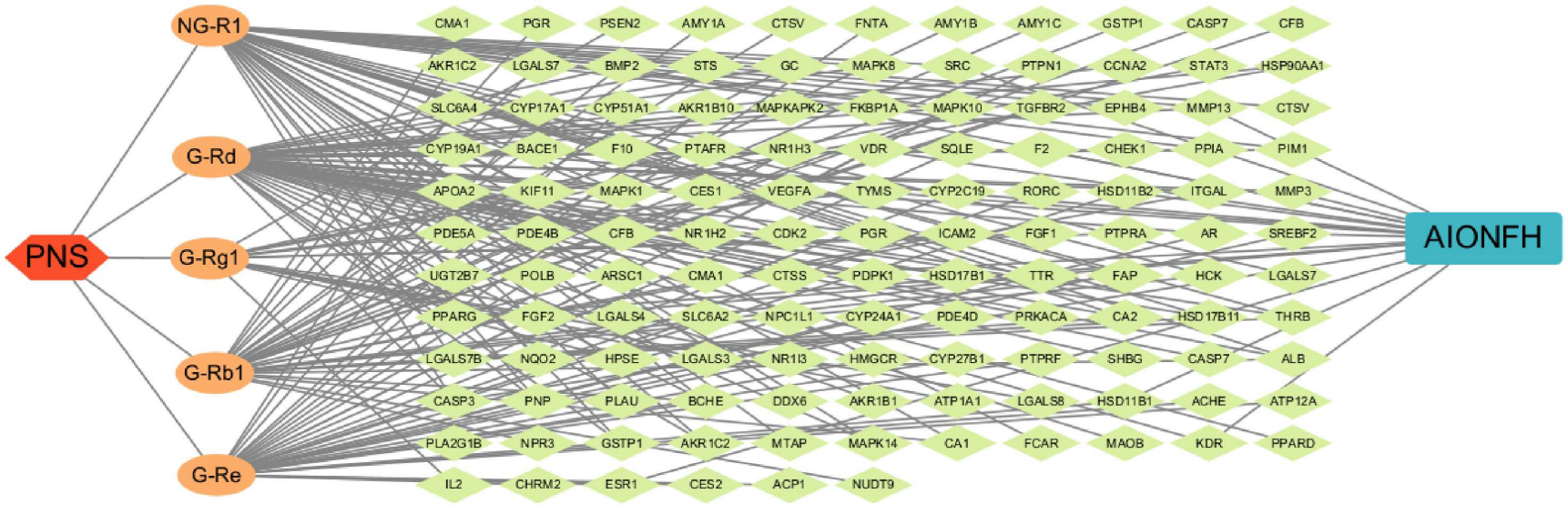
Table 3 | Contribution values of residual free energy

residu	Energy (kcal/mol）
ARG:208	-0.958
LYS:211	-1.559
ALA:212	-1.72
VAL:215	-0.971
PHE:227	-0.197
THR:231	-0.243
VAL:234	-0.613
ASP:323	-2.679
ALA:324	-0.67
LEU:326	-1.281
GLY:327	-1.004
LEU:330	-0.715
LEU:346	-0.332
ALA:349	-0.321
GLU:353	-1.568

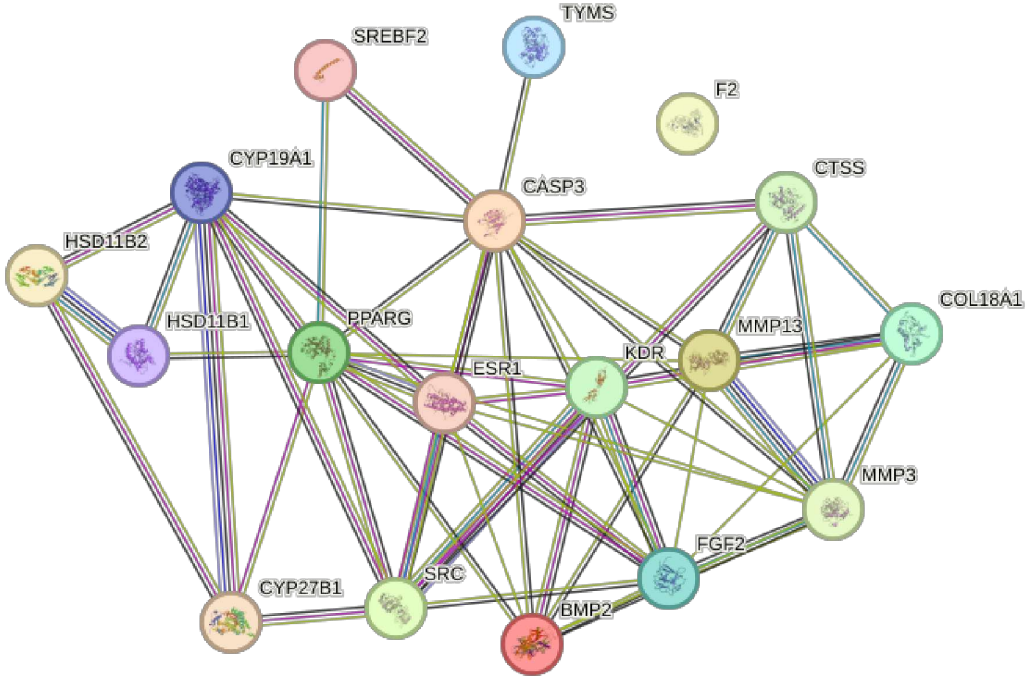
A


drug
AIONFH
101
18
672
Size of each list
690
345
0
119
690
drug
AIONFH
Number of elements: specific (1) or shared by 2, 3, ... lists
773
2 (18)
1

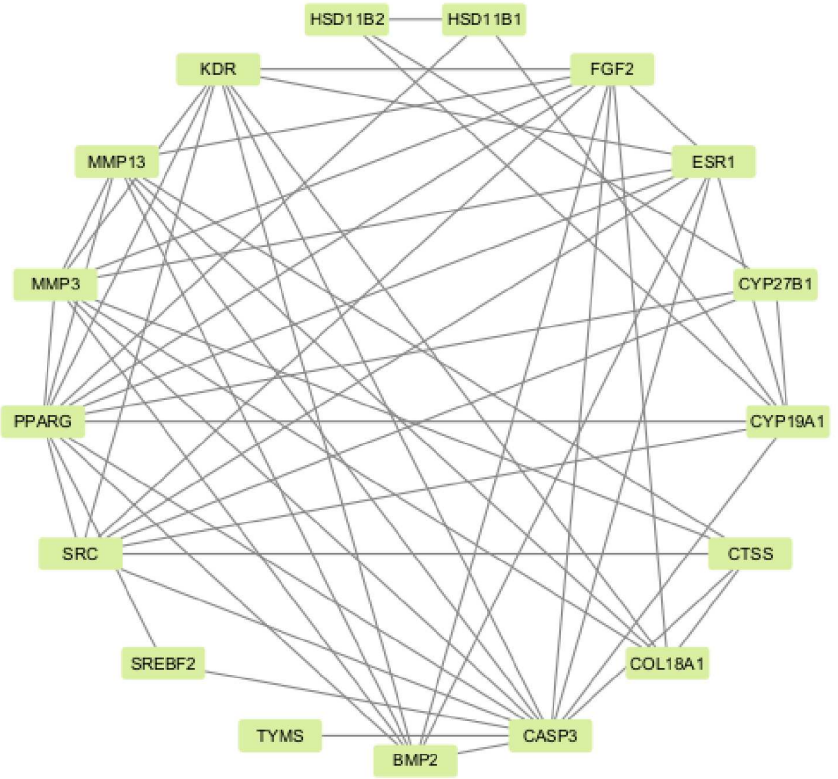
B


PNS
NG-R1
G-Rd
G-Rg1
G-Rb1
G-Re
AIONFH
CMA1 PGR PSEN2 AMY1A CTSV FNTA AMY1B AMY1C GSTP1 CASP7 CFB
AKR1C2 LGALS7 BMP2 STS GC MAPK8 SRC PTPN1 CCNA2 STAT3 HSP90AA1
SLC6A4 CYP17A1 CYP51A1 AKR1B10 MAPKAPK2 FKBP1A MAPK10 TGFBR2 EPHB4 MMP13 CTSV
CYP19A1 BACE1 F10 PTAFR NR1H3 VDR SQLE F2 CHEK1 PPIA PIM1
APOA2 KIF11 MAPK1 CES1 VEGFA TYMS CYP2C19 RORC HSD11B2 ITGAL MMP3
PDE5A PDE4B CFB NR1H2 CDK2 PGR ICAM2 FGF1 PTPRA AR SREBF2
UGT2B7 POLB ARSC1 CMA1 CTSS PDPK1 HSD17B1 TTR FAP HCK LGALS7
PPARG FGF2 LGALS4 SLC6A2 NPC1L1 CYP24A1 PDE4D PRKACA CA2 HSD17B11 THRB
LGALS7B NQO2 HPSE LGALS3 NR1I3 HMGCR CYP27B1 PTPRF SHBG CASP7 ALB
CASP3 PNP PLAU BCHE DDX6 AKR1B1 ATP1A1 LGALS8 HSD11B1 ACHE ATP12A
PLA2G1B NPR3 GSTP1 AKR1C2 MTAP MAPK14 CA1 FCAR MAOB KDR PPARD
IL2 CHRM2 ESR1 CES2 ACP1 NUDT9

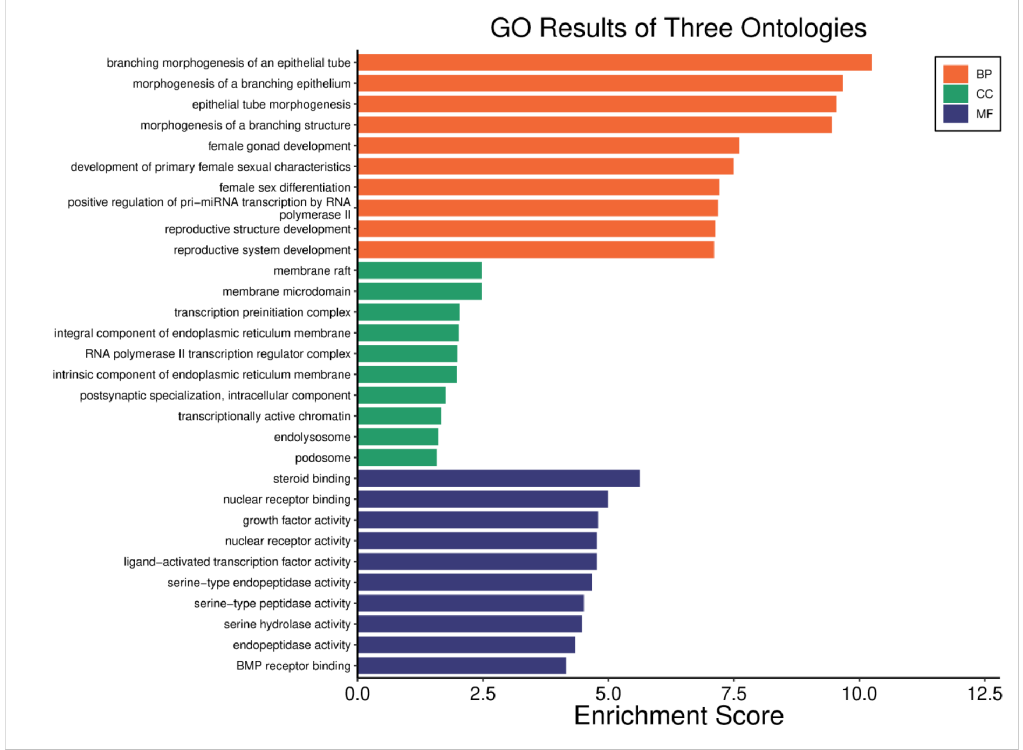
A


SREBF2
TYMS
F2
CYP19A1
CASP3
CTSS
HSD11B2
COL18A1
HSD11B1
PPARG
MMP13
ESR1
KDR
MMP3
FGF2
SRC
CYP27B1
BMP2

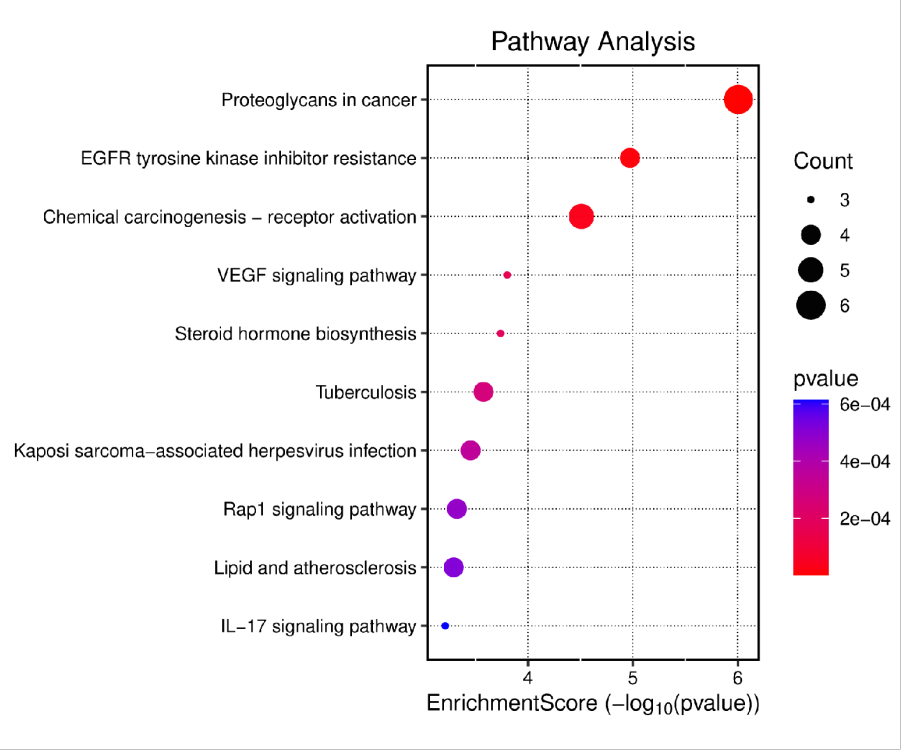
B


HSD11B2
HSD11B1
KDR
FGF2
MMP13
ESR1
MMP3
CYP27B1
PPARG
CYP19A1
SRC
CTSS
SREBF2
COL18A1
TYMS
CASP3
BMP2

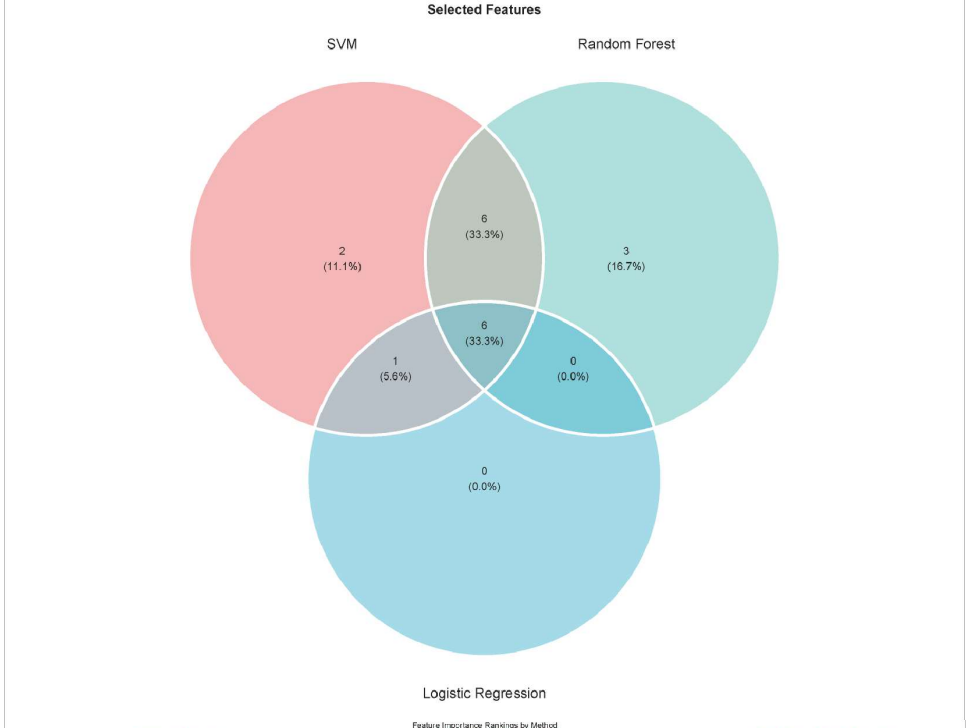
A


GO Results of Three Ontologies
branching morphogenesis of an epithelial tube
morphogenesis of a branching epithelium
epithelial tube morphogenesis
morphogenesis of a branching structure
female gonad development
development of primary female sexual characteristics
female sex differentiation
positive regulation of pri−miRNA transcription by RNA polymerase II
reproductive structure development
reproductive system development
membrane raft
membrane microdomain
transcription preinitiation complex
integral component of endoplasmic reticulum membrane
RNA polymerase II transcription regulator complex
intrinsic component of endoplasmic reticulum membrane
postsynaptic specialization, intracellular component
transcriptionally active chromatin
endolysosome
podosome
steroid binding
nuclear receptor binding
growth factor activity
nuclear receptor activity
ligand−activated transcription factor activity
serine−type endopeptidase activity
serine−type peptidase activity
serine hydrolase activity
endopeptidase activity
BMP receptor binding
BP
CC
MF
0.0
2.5
5.0
7.5
10.0
12.5
Enrichment Score

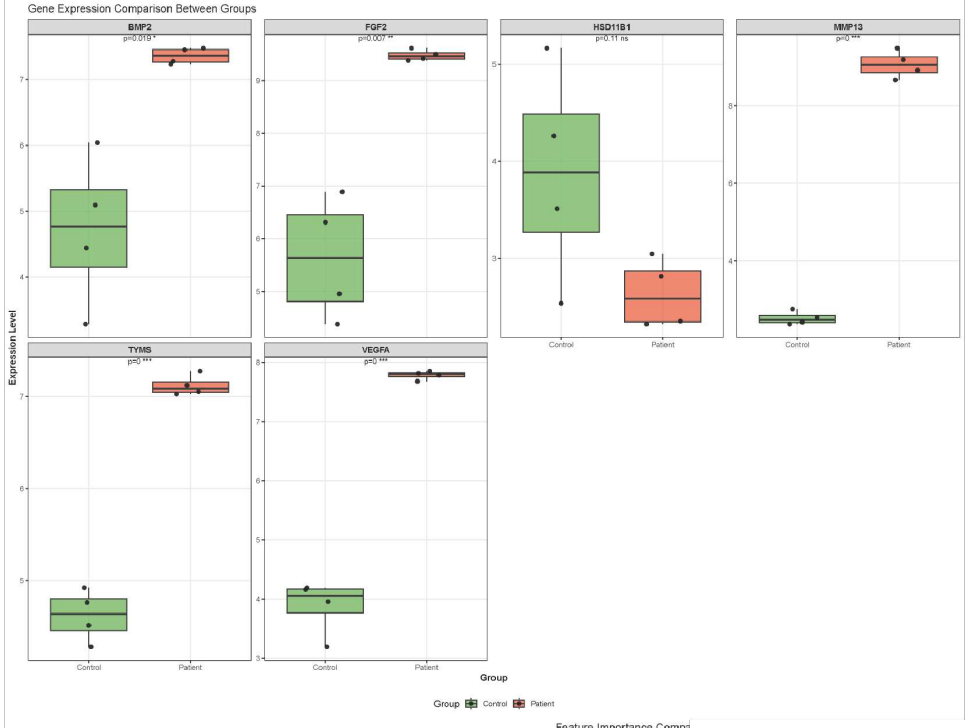
B


Pathway Analysis
Proteoglycans in cancer
EGFR tyrosine kinase inhibitor resistance
Chemical carcinogenesis − receptor activation
VEGF signaling pathway
Steroid hormone biosynthesis
Tuberculosis
Kaposi sarcoma−associated herpesvirus infection
Rap1 signaling pathway
Lipid and atherosclerosis
IL−17 signaling pathway
4
5
6
EnrichmentScore (−log10(pvalue))
Count
3
4
5
6
pvalue
6e−04
4e−04
2e−04

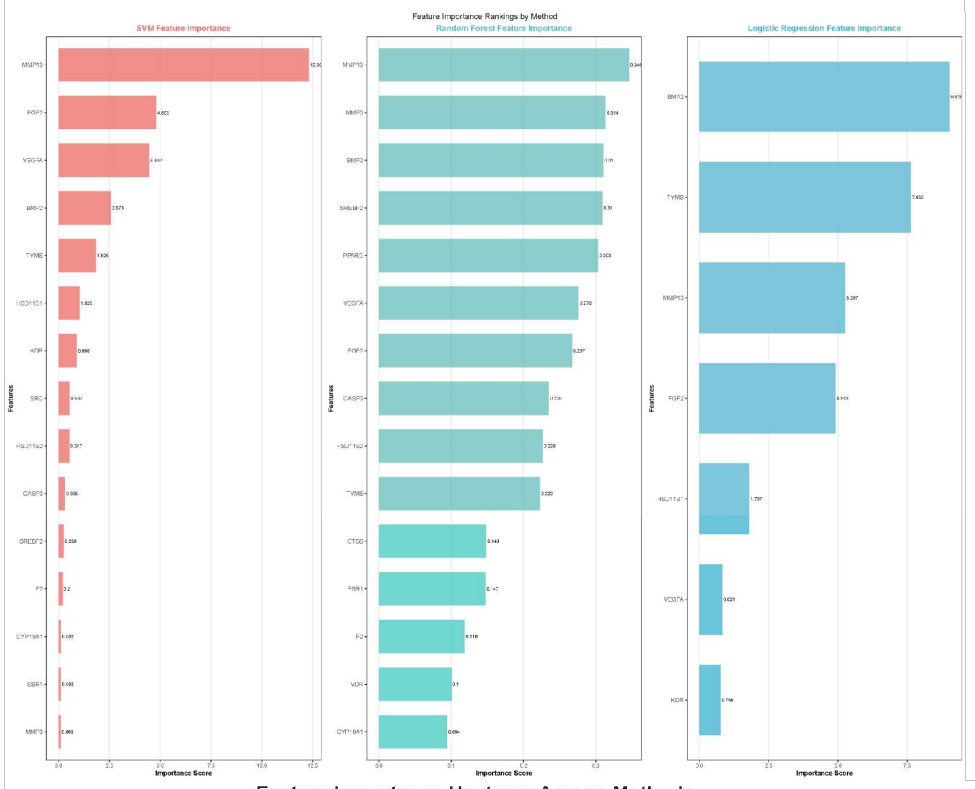
A


Selected Features
SVM
Random Forest
Logistic Regression
2
(11.1%)
6
(33.3%)
3
(16.7%)
6
(33.3%)
1
(5.6%)
0
(0.0%)
0
(0.0%)

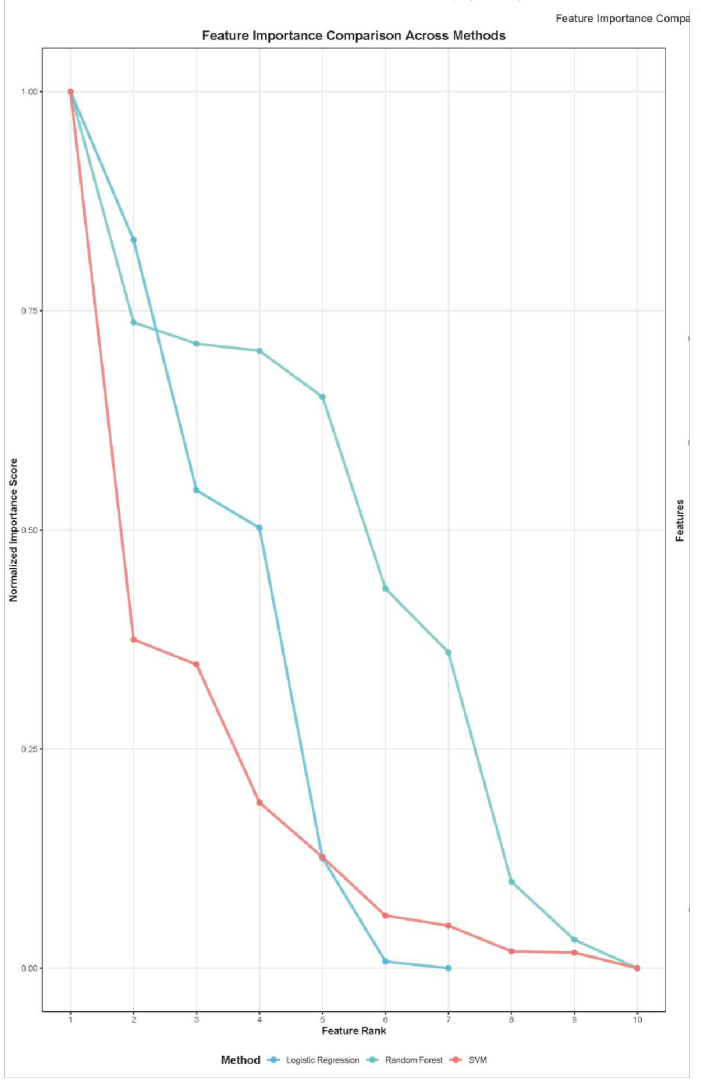
B


Gene Expression Comparison Between Groups
BMP2
FGF2
HSD11B1
MMP13
TYMS
VEGFA
Expression Level
Control
Patient
Group

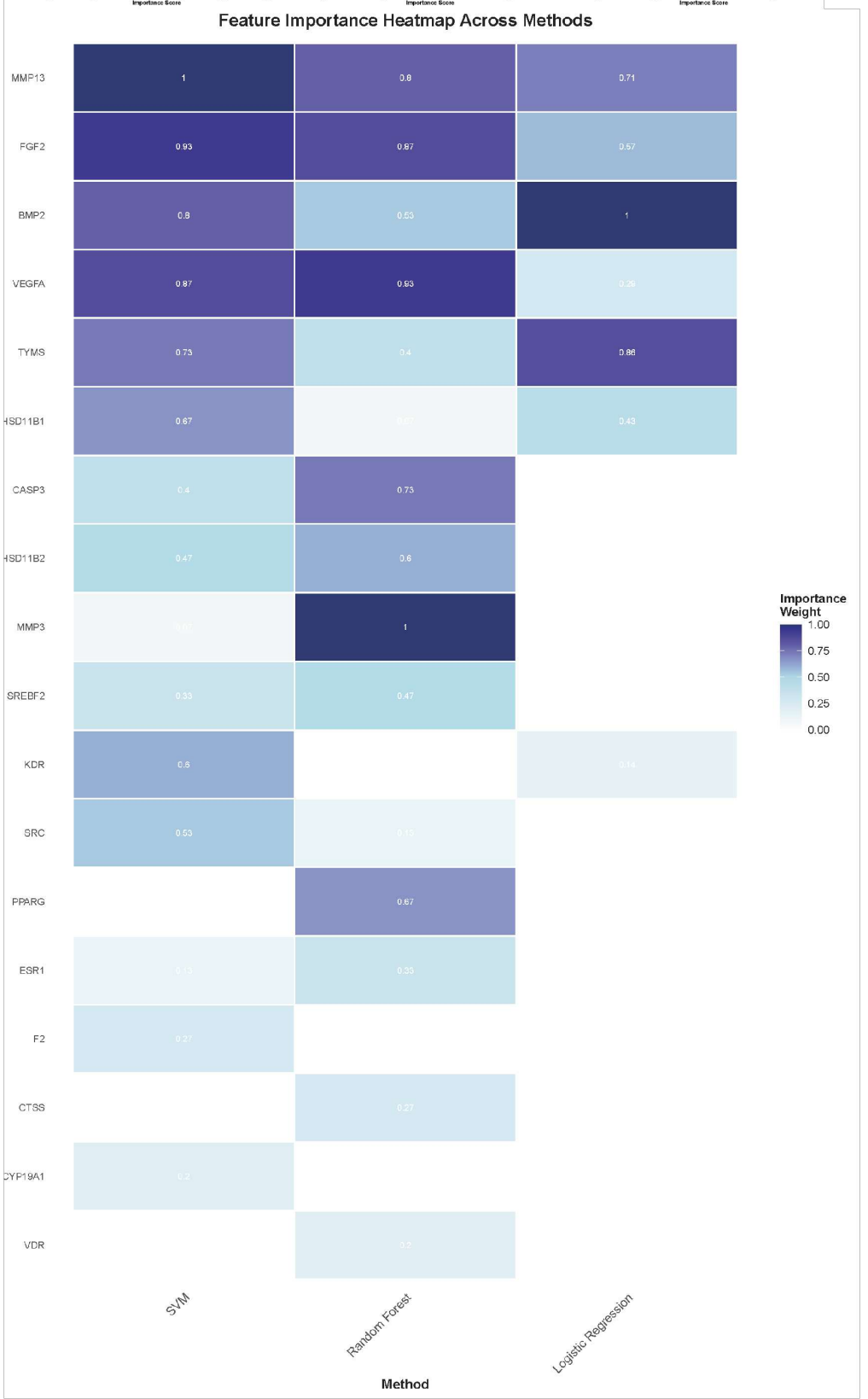
C

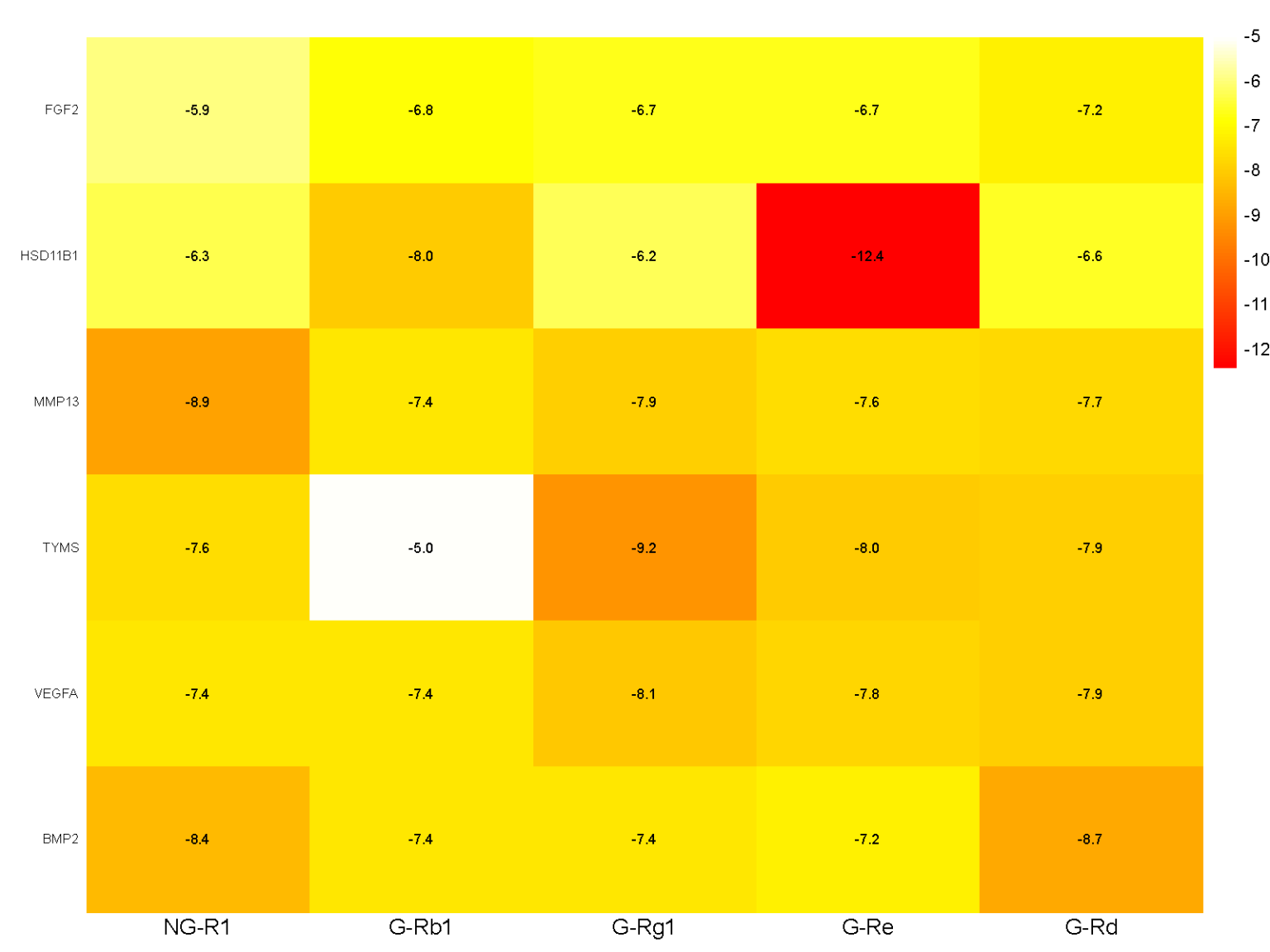

Feature Importance Rankings by Method
SVM Feature Importance
Random Forest Feature Importance
Logistic Regression Feature Importance
Importance Score
Features

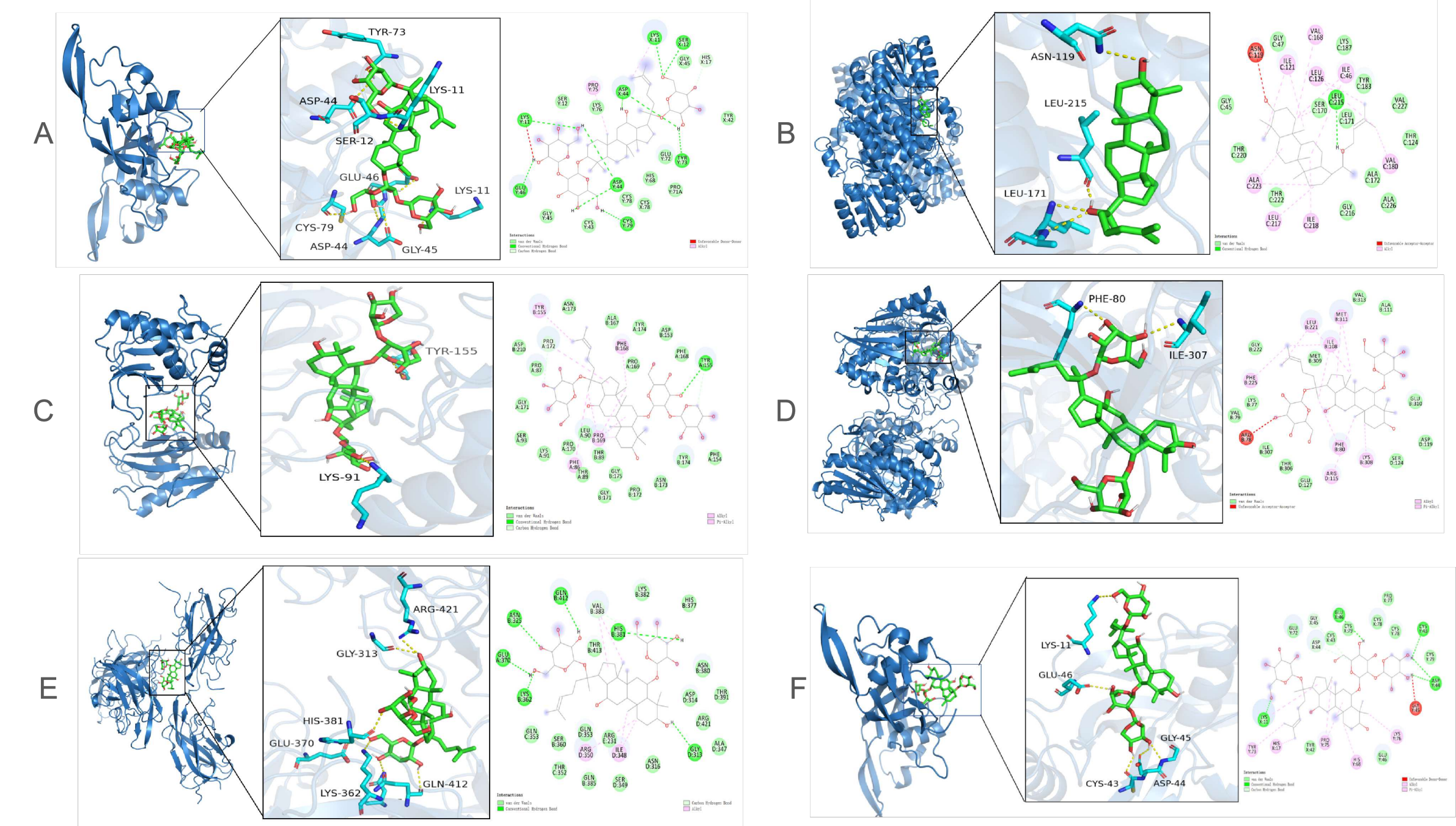
D

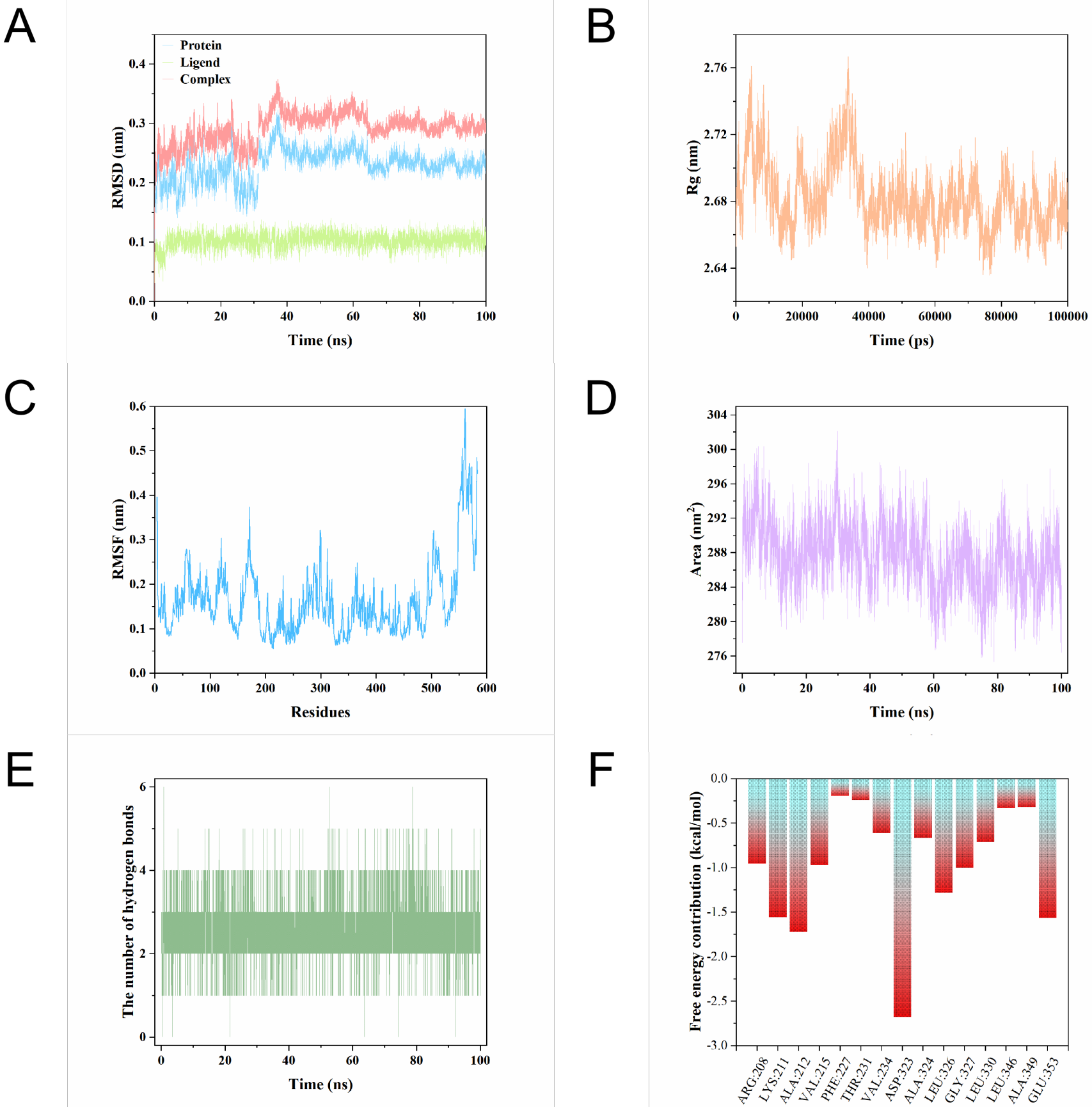

Feature Importance Comparison Across Methods
Normalized Importance Score
Feature Rank
Method
Logistic Regression
Random Forest
SVM
Features

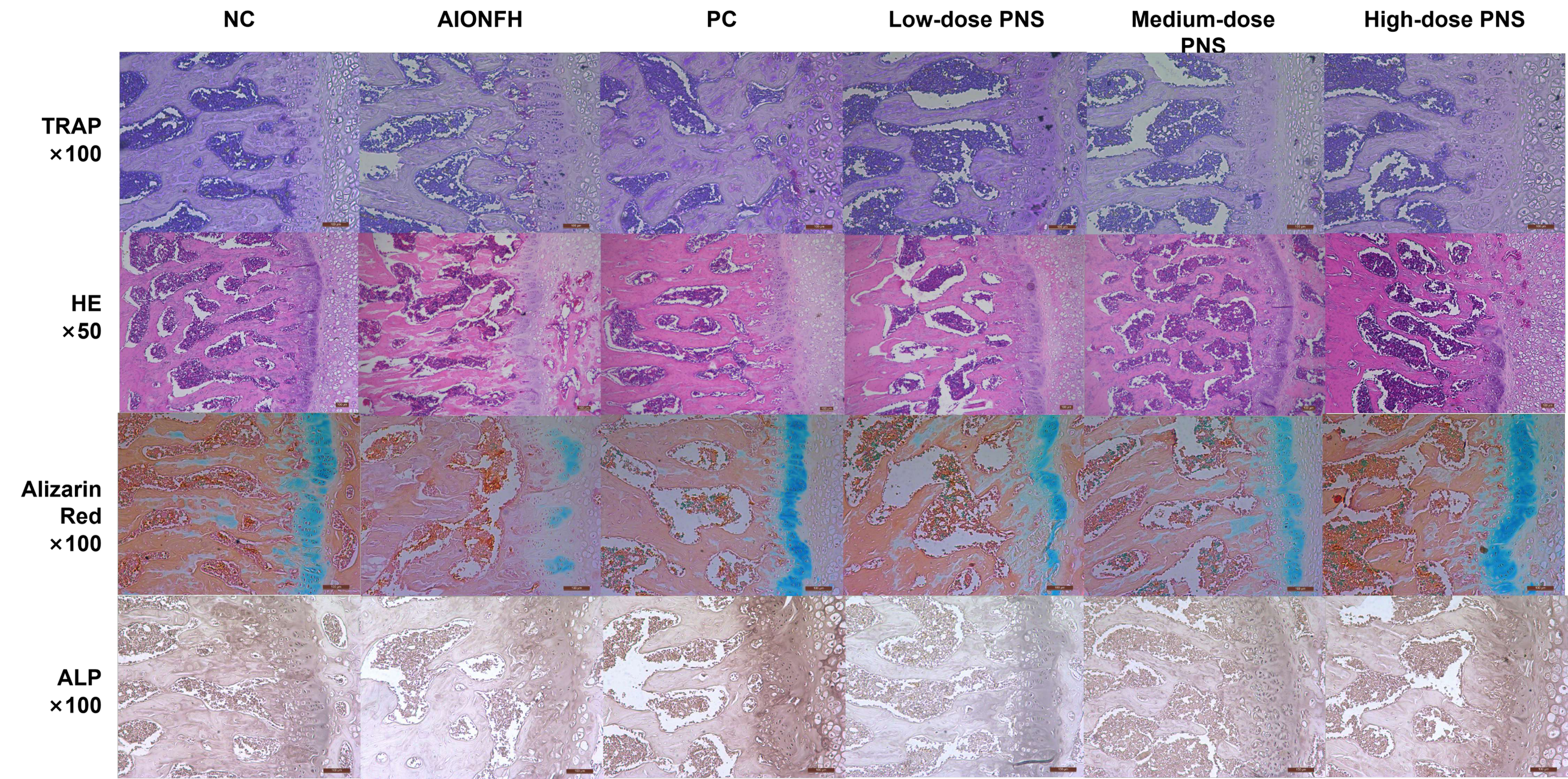
E

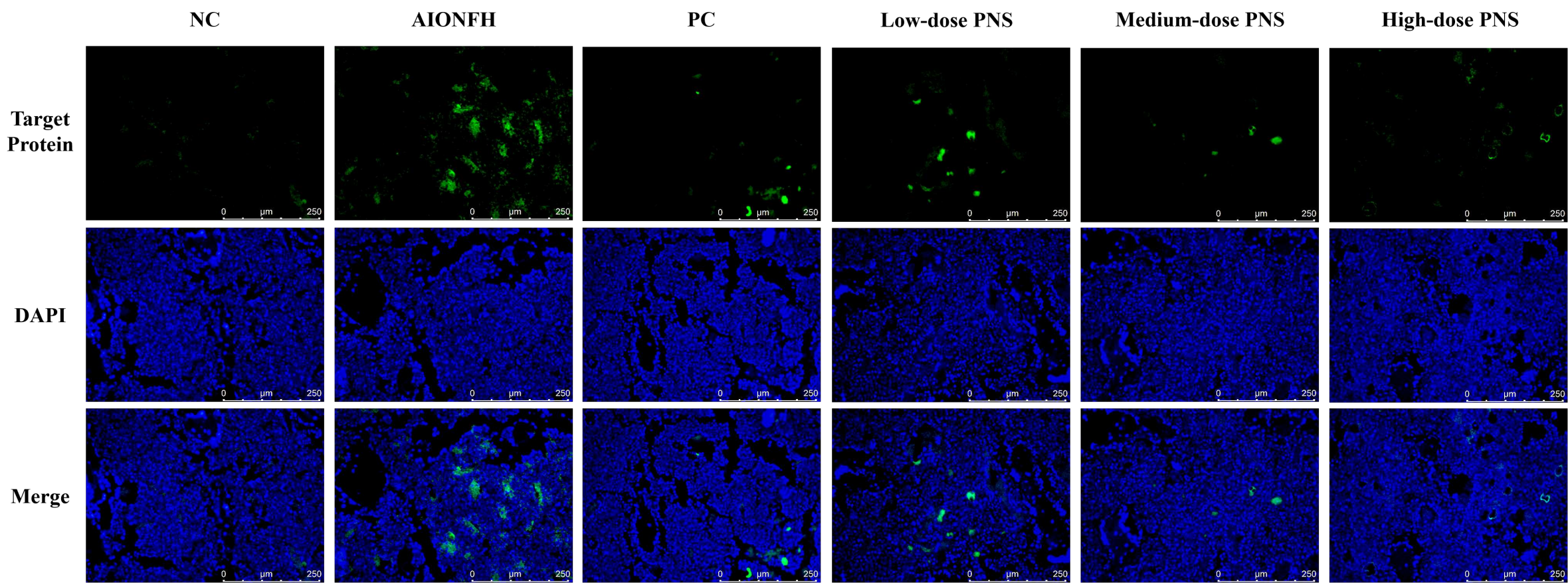

Feature Importance Heatmap Across Methods
MMP13
FGF2
BMP2
VEGFA
TYMS
HSD11B1
CASP3
HSD11B2
MMP3
SREBF2
KDR
SRC
PPARG
ESR1
F2
CTSS
CYP19A1
VDR
SVM
Random Forest
Logistic Regression
Method
Importance Weight
1.00
0.75
0.50
0.25
0.00


FGF2
HSD11B1
MMP13
TYMS
VEGFA
BMP2
-5.9
-6.8
-6.7
-6.7
-7.2
-6.3
-8.0
-6.2
-12.4
-6.6
-8.9
-7.4
-7.9
-7.6
-7.7
-7.6
-5.0
-9.2
-8.0
-7.9
-7.4
-7.4
-8.1
-7.8
-7.9
-8.4
-7.4
-7.4
-7.2
-8.7
NG-R1
G-Rb1
G-Rg1
G-Re
G-Rd
-5
-6
-7
-8
-9
-10
-11
-12

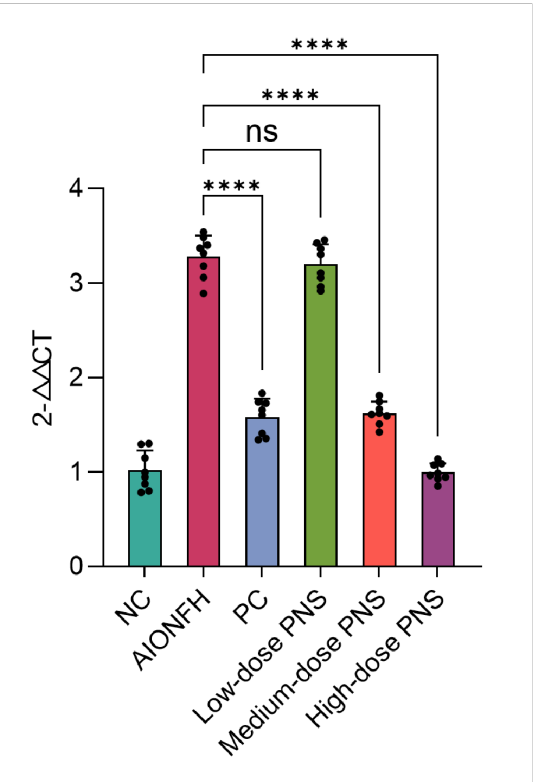

A
TYR-73
ASP-44
LYS-11
SER-12
GLU-46
LYS-11
CYS-79
ASP-44
GLY-45
B
ASN-119
LEU-215
LEU-171
C
TYR-155
LYS-91
D
PHE-80
ILE-307
E
ARG-421
GLY-313
HIS-381
GLU-370
LYS-362
GLN-412
F
LYS-11
GLU-46
GLY-45
CYS-43
ASP-44


A
Protein
Ligend
Complex
RMSD (nm)
Time (ns)
B
Rg (nm)
Time (ps)
C
RMSF (nm)
Residues
D
Area (nm^2)
Time (ns)
E
The number of hydrogen bonds
Time (ns)
F
Free energy contribution (kcal/mol)
ARG:208
LYS:211
ALA:212
VAL:215
PHE:227
THR:231
VAL:234
ASP:323
ALA:324
LEU:326
GLY:327
LEU:330
LEU:346
ALA:349
GLU:353

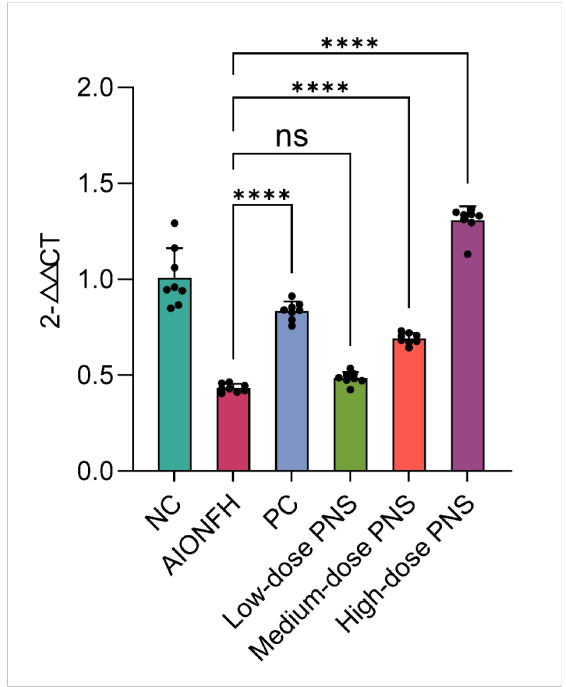

NC
AIONFH
PC
Low-dose PNS
Medium-dose PNS
High-dose PNS
TRAP ×100
HE ×50
Alizarin Red ×100
ALP ×100


NC
AIONFH
PC
Low-dose PNS
Medium-dose PNS
High-dose PNS
Target Protein
DAPI
Merge
0 μm 250

HSD11B1



Runx2



CTSK

